

# Margin-Based Generalisation Bounds for Quantum Kernel Methods under Local Depolarising Noise

S. Govender<sup>1</sup> and I. Sinayskiy<sup>1,2</sup>

<sup>1</sup>Discipline of Physics, School of Agriculture and Science, University of KwaZulu-Natal, Durban 4001, South Africa

<sup>2</sup>National Institute for Theoretical and Computational Sciences (NITheCS), Stellenbosch, South Africa.

## Abstract

Generalisation refers to the ability of a machine learning (ML) model to successfully apply patterns learned from training data to new, unseen data. Quantum devices in the current Noisy Intermediate-Scale Quantum (NISQ) era are inherently affected by noise, which degrades generalisation performance. In this work, we derive upper and lower margin-based generalisation bounds for Quantum Kernel-Assisted Support Vector Machines (QSVMs) under local depolarising noise. These theoretical bounds characterise noise-induced margin decay and are validated via numerical simulations across multiple datasets, as well as experiments on real quantum hardware. We further justify the focus on margin-based measures by empirically establishing margins as a reliable indicator of generalisation performance for QSVMs. Additionally, we motivate the study of local depolarising noise by presenting empirical evidence demonstrating that the commonly used global depolarising noise model is overly optimistic and fails to accurately capture the degradation of generalisation performance observed in the NISQ era.

## 1 Introduction

The field of quantum machine learning (QML) lies at the intersection of quantum computing and classical machine learning (CML) [1]. As such, QML has inherited fundamental questions from both these fields, one critical question being generalisation.

Generalisation is defined as the ability of a machine learning model to learn patterns from some initial training dataset and consequently apply those patterns to make accurate predictions on a related, never-before-encountered dataset. Generalisation has been well-studied in the field of CML and has been quantified using several measures [2–6]. Particularly, much work has been put into developing a strong theory of generalisation for classical support vector machines (SVMs) [2, 3, 6–10], since their introduction by Cortes and Vapnik [11].

However, some of the conventional expectations of

generalisation in CML do not translate directly to QML, due to quantum effects such as superposition, entanglement, and device noise present in the current Noisy Intermediate Scale Quantum (NISQ) era [12]. Consequently, generalisation in QML remains a relatively under-explored field.

Recent work involving near-term QML models has revealed unexpected generalisation behaviour, which has challenged the applicability of traditional uniform generalisation bounds to near-term models [13, 14]. These results suggest that a revised approach is required to study the generalisation performance of current QML models.

Margin-based metrics have since become a promising alternative to studying generalisation. Empirical evidence has shown that margin-based generalisation measures outperform conventional metrics as reliable predictors of generalisation performance for Quantum Neural Networks (QNNs) [15]. However, margins have

not yet been explored for Quantum-Kernel-Assisted Support Vector Machines (QSVMs).

Device noise presents an additional challenge in the study of generalisation in the NISQ era as it limits the performance of QML models. This type of noise is unavoidable and can be modelled using the depolarising noise model. A quantum state affected by maximum depolarising noise reduces to its maximally mixed state, losing all useful information about the state and making the learning task impossible. This challenge has since led to the study of the predictive power of modern QML models under noise [16–18].

However, these studies primarily focus on the global depolarising model, which applies noise to all qubits in the system simultaneously. This model, while analytically tractable does not reflect real device noise as accurately as the local depolarising noise model, which applies noise independently to each qubit [19]. The local depolarising noise model remains relatively unexplored in terms of generalisation and QSVMs. The ability to accurately understand how the generalisation performance of QSVMs is influenced by noise will provide vital insight into their predictive performance in the NISQ era.

In this work, we derive analytical bounds to quantify the effect of local depolarising noise on quantum kernel values, and present formal upper and lower bounds on QSVM margins under local depolarising noise based on SVM optimality relations. These bounds are validated through numerical simulations and experiments on real quantum hardware and demonstrate the robustness of QSVMs under noise. We further establish a strong correlation between margin-based metrics and QSVM generalisation performance in the ideal (noiseless) scenario to justify our margin-based analysis. Additionally, we motivate the study of local depolarising noise by empirically establishing that studying local (per-qubit) depolarisation noise is of greater benefit to understanding generalisation in the NISQ era than global depolarising noise.

The paper is structured as follows. Sections 2 and 3 present a literature review and provide a necessary introduction into margin theory for classical and quantum-enhanced SVMs. Section 4 presents empirical evidence showing margins as a reliable generalisation measure in the ideal scenario. Section 5 includes empirical ev-

idence for the study of local depolarising noise. The main results of the paper are presented in Section 6. Numerical experiments validating these results are presented in Section 7. Section 8 concludes the paper.

## 2 Literature Review

Generalisation theory for classical Support Vector Machines (SVMs) is relatively well-developed. Following the introduction of SVMs by Cortes and Vapnik [11], foundational work by Bartlett and Shawe-Taylor [7] established generalisation guarantees for SVMs using margins. Following this, Vapnik and Chapelle [9] derived generalisation bounds that were independent of the feature space dimensionality but dependent on the expected number of support vectors. These results built upon the Vapnik-Chervonenkis (VC) theory, in which the VC-dimension quantified the complexity of a hypothesis class and provided uniform generalisation bounds [8].

Soon after, bounds were presented by Bartlett and Mendelson [20] using the Rademacher complexity measure, which were further strengthened through PAC-Bayesian margin bounds [2–4]. More recently, these bounds were revisited and improved by Grønlund et al. [6], who presented a near-tight upper bound and a complementary lower bound for the generalisation performance of classical SVMs in terms of margins.

Several analogous measures of generalisation have been explored within QML. These include bounds based on pseudo-dimension, the quantum Fisher information metric, and other metrics from quantum information theory [21–23]. Bu et al. [24] studied Rademacher complexity in parametrised quantum circuits [24–26], with [26] exploring the effects of noise in the quantum circuit. A comprehensive overview of generalisation measures and error bounds for QML models in the NISQ era can be found in [18].

Recently, traditional claims based on uniform generalisation bounds have been challenged by Zhang et al. [27], who have demonstrated the memorisation abilities of modern deep learning models through systematic randomisation experiments. This work was later built upon by Gil-Fuster et al. [14], who performed similar experiments using randomly labelled data for near-term QNNs. Their results ultimately exposed the limitations

of uniform generalisation bounds when applied to near-term models.

Further unexpected generalisation behaviour was observed by Caro et al. [13], who found strong generalisation performance in QML models trained on small datasets, challenging the conventional assumption that generalisation requires large training sets. These works have significantly highlighted the need to find alternative approaches to studying generalisation theory for QML.

This resulted in alternative data set-dependent measures, such as margin-based metrics [15, 28] used to explore generalisation performance, becoming increasingly important for analysing learning performance.

Several studies have further investigated the robustness of QML models in the presence of noise [16, 17, 29]. Thanaisilp et al. [29] demonstrated that under specific conditions, quantum kernel values can become exponentially concentrated towards some fixed value, leading to trivial models and inaccurate predictions. These studies are therefore vital to understanding the generalisation performance of near-term QML models in the NISQ era.

### 3 Preliminaries

#### 3.1 SVM Theory

In the simplest case, to perform binary classification on linearly separable data using a linear classifier, the SVM algorithm attempts to find a hyperplane (a line) that effectively separates data points belonging to two different classes. For separable data, infinitely many hyperplanes exist that could satisfy this criterion; hence, by solving an optimisation problem, the SVM algorithm locates the optimal separating hyperplane such that the distance from the hyperplane to the nearest data points from each class is maximised.

This distance is termed the geometric margin, which is defined as the minimum Euclidean distance from all points to the hyperplane. The closest data points to the hyperplane are referred to as support vectors.

For the linearly separable case, this hyperplane is a line, with the equation  $w \cdot x + b = 0$ . Here,  $w$  is termed the weight vector, and is perpendicular (normal) to the hyperplane.  $b$  is the bias term (or intercept), which shifts

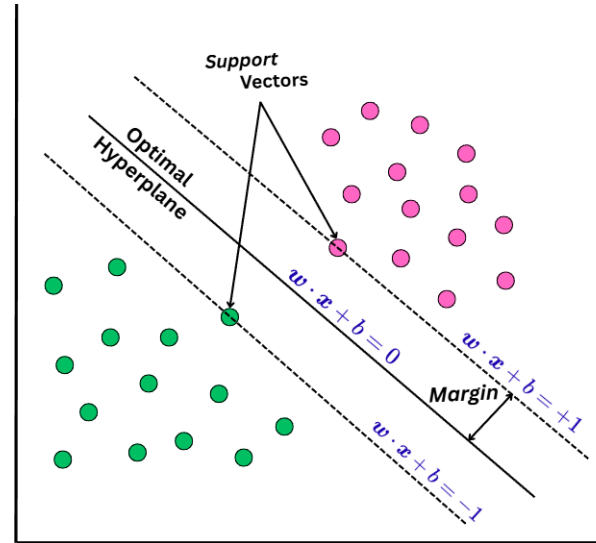


Figure 1: Diagram depicting the optimal linear hyperplane returned by an SVM to separate two classes of data points (green and pink circles). The support vectors used to determine the hyperplane and the corresponding geometric margin are labelled. The equations of the separating and marginal hyperplanes are depicted in blue. A hard margin is depicted here since all samples are classified with a distance greater than the geometric margin away from the separating hyperplane.

the hyperplane away from the origin.

The functional (confidence) margin of a classifier  $f$  at point  $x_i$  is defined as  $y_i f(x_i)$  where  $y_i \in \{-1, +1\}$  is the true label of the point  $x_i$  [5].

For binary classification problems, the SVM classifier returns the hypothesis  $f \rightarrow \text{sign}(w \cdot x + b)$ , such that all points of one class are given a positive value and are placed on one side of the hyperplane, whereas the points belonging to the other class hold a negative value and fall on the other side of the hyperplane.

In this way, it is clear that when  $y_i f(x_i) > 0$ , the sample has been correctly classified.

For real-valued functions,  $f$ , functional margins can be calculated using hypotheses returned as  $f \rightarrow w \cdot x + b$ . In this case, the magnitude  $|f(x_i)|$  represents the confidence of the prediction made by the classifier [5]. In

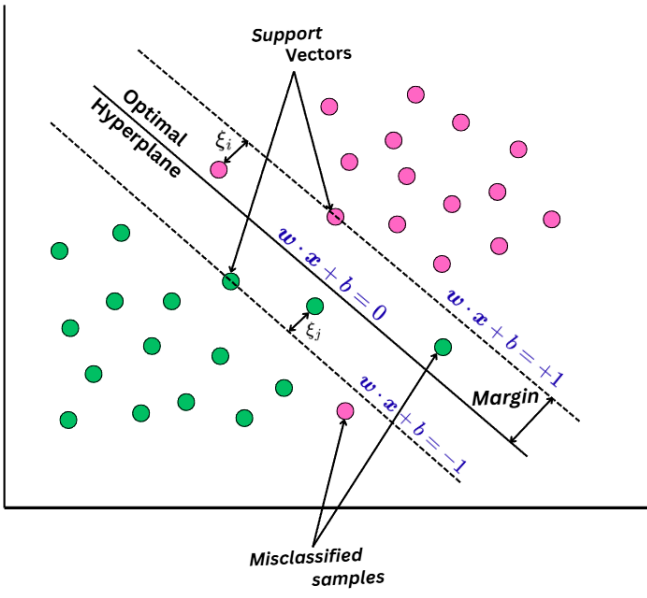


Figure 2: Diagram depicting the optimal linear hyperplane returned by the SVM to separate the two classes of data points (green and pink circles). The equations of the separating and marginal hyperplanes are depicted in blue. A soft margin is depicted here since some points are classified on the correct side of the linear hyperplane but with distances  $1 - \xi_i$  and  $1 - \xi_j$  from the separating hyperplane. Misclassified points which are placed on the wrong side of the hyperplane are also labelled.

in the linearly separable case, the functional and geometric margins are related for the training sample  $x_i$  as:  $|y_i f(x_i)| \geq \gamma_{\text{geom}} \|\mathbf{w}\|$ , where  $\|\cdot\|$  represents the Euclidean norm and is defined in more detail at the end of the section.

Through rescaling of the real-valued classifier output, detailed in [5], the maximum geometric margin takes the form:

$$\gamma = \max_{(\mathbf{w}, b)} \frac{1}{\|\mathbf{w}\|} \quad (1)$$

with  $y_i(\mathbf{w} \cdot \mathbf{x}_i + b) \geq 1$  for the maximising pair  $(\mathbf{w}, b)$ .

Figure 1 depicts the optimal hyperplane that separates two distinct classes (green and pink circles), and in doing so, obtains the maximal margin. The marginal

hyperplanes, with equations  $\mathbf{w} \cdot \mathbf{x} + b = \pm 1$  are shown parallel to the separating hyperplane and the support vectors used to determine the margin are portrayed accordingly.

In the case where the samples corresponding to each class can not be linearly separated, then the previously discussed constraints may not hold.

This case is illustrated in Figure 2, which depicts misclassified samples and samples from each class correctly classified, but with a Euclidean distance that is less than the maximum margin distance from the hyperplane.

There are two formalisms which describe the optimisation problem defining the SVM algorithm; namely the primal and dual formalisms.

The primal optimisation problem for the non-separable case has the form:

$$\min_{\mathbf{w}, b, \xi} \frac{1}{2} \|\mathbf{w}\|^2 + C \sum_{i=1}^m \xi_i \quad (2)$$

where  $r = 1$  for the hinge loss function, which is widely used for SVMs, and with the constraints

$$y_i(\mathbf{w} \cdot \phi(\mathbf{x}_i) + b) \geq 1 - \xi_i \text{ and } \xi_i \geq 0 \text{ for } i \in [1, m]$$

Here,  $\xi = (\xi_1 \dots \xi_m)^T$  represents the slack variable where  $\xi_i$  is the distance by which vector  $\mathbf{x}_i$  crossed the specified marginal hyperplane. Vectors with positive slack values may be considered outliers.  $C$  represents the trade-off between maximising the margin and minimising the amount of slack due to outliers. Higher  $C$  values correspond to stricter penalties for misclassifications than smaller  $C$  values.

The maximal margin obtained in this case is termed the soft margin, since it allows some slack due to outliers. The margin for the linearly separable case is denoted the hard margin and does not allow for slack.

A Lagrangian is defined for the dual formalism as

$$\mathcal{L}(\mathbf{w}, b, \alpha) = \sum_{i,j=1}^m \alpha_i \alpha_j y_i y_j (\mathbf{x}_i \cdot \mathbf{x}_j) \quad (3)$$

with the Lagrangian variables  $\alpha = (\alpha_1, \dots, \alpha_m)^T$ , where  $\alpha_i \geq 0$ ,  $i \in \{1, \dots, m\}$  and  $m$  is the number of constraints.

The above Lagrangian can be used to obtain the Karush-Kuhn-Tucker (KKT) conditions for the non-separable case as:

$$\mathbf{w} = \sum_{i=1}^m \alpha_i y_i \phi(\mathbf{x}_i) \quad (4)$$

$$0 = \sum_{i=1}^m \alpha_i y_i \quad (5)$$

$$C = \alpha_i + \beta_i \quad (6)$$

$$\alpha_i = 0 \text{ or } y_i(\mathbf{w} \cdot \phi(\mathbf{x}_i) + b) = 1 - \xi_i \quad (7)$$

$$\beta_i = 0 \text{ or } \xi_i = 0 \quad (8)$$

The complete derivation of these conditions can be found in [5].

It is clear from the penultimate condition that for all non-zero  $\alpha_i$  variables, the associated  $\mathbf{x}_i$  vectors lie on the marginal hyperplanes and therefore must be support vectors. Additionally, in this case, if  $\xi_i = 0$ , the condition reduces to that of the separable case, and the support vector  $\mathbf{x}_i$  lies on the marginal hyperplane. However, if  $\xi_i \neq 0$ , then the support vector  $\mathbf{x}_i$  is an outlier (as depicted in Figure 2). Furthermore, the last condition implies that  $\beta_i = 0$  in this case, which further implies that  $\alpha_i = C$  for the non-separable case.

The dual Lagrangian function has been largely studied since it can be easily modified to accommodate the famous kernel trick [30] by replacing the dot product of the support vectors with the kernel element associated with them in the SVM algorithm. This enables the algorithm to utilise a feature map to map the data to a higher-dimensional space (feature space) in which a hyperplane (higher-dimensional surface) can be found in order to separate the data. The kernel trick is beneficial since there is no need to explicitly define the feature map,  $\Phi(\cdot)$ . It is only necessary to determine the inner product in this space.

Modifying equation (3) to include the kernel results in the form

$$\mathcal{L}(\alpha, K) = \sum_{i,j=1}^m \alpha_i - \frac{1}{2} \sum_{i,j=1}^m \alpha_i \alpha_j y_i y_j K(\mathbf{x}_i, \mathbf{x}_j) \quad (9)$$

where  $K(\mathbf{x}_i, \mathbf{x}_j)$  computes the kernel value for samples  $\mathbf{x}_i$  and  $\mathbf{x}_j$ . Additionally, we can define the squared Euclidean norm of the weight vector in the feature space

as,  $\|\mathbf{w}\|^2 = \sum_{i,j=1}^m \alpha_i \alpha_j y_i y_j K(\mathbf{x}_i, \mathbf{x}_j)$ . The inverse of this quantity yields the squared geometric margin.

### 3.2 QSVM Theory

Notably, the kernel trick, and by extension, kernel methods are essential for QSVMs. QSVMs use quantum circuits run on a quantum computer to obtain a matrix of kernel values [31]. These matrix elements are computed as the squared state overlap between two feature vectors corresponding to two data points. These kernel elements take the form:

$$K(\mathbf{x}_i, \mathbf{x}_j) = |\langle \Phi(\mathbf{x}_j) | \Phi(\mathbf{x}_i) \rangle|^2 \quad (10)$$

where  $|\Phi(\mathbf{x}_i)\rangle$  defines a feature map, which maps the classical data point  $\mathbf{x}_i$  to a higher-dimensional Hilbert space.

The Hilbert-Schmidt inner product [19] can be used to calculate the kernel elements for mixed states as,  $K(\mathbf{x}_i, \mathbf{x}_j) = \text{Tr}(\rho(\mathbf{x}_i) \rho(\mathbf{x}_j))$ .

Notably, the computation of the matrix of the quantum kernel values is the only process run on the quantum computer. The quantum kernel (Gram) matrix is then used by the SVM algorithm in a manner identical to the classical formalism. In this way, the resulting QSVM algorithm is denoted as a hybrid quantum-classical ML algorithm.

### 3.3 Depolarising Noise Models

A depolarising noise channel is a completely positive trace-preserving (CPTP) map that maps a quantum state onto a maximally mixed state with some finite probability [19].

Global depolarising noise channels are applied to the entire system of qubits simultaneously, whereas local depolarising noise channels are applied to each qubit in a system, individually and thus capture entanglement and other qubit-qubit interactions in the system.

The resulting  $N$ -qubit state after the application of a global depolarising channel is given by the following expression:

$$\mathcal{E}_G(\rho) = (1 - p_G)\rho + p_G \frac{I}{2^N} \quad (11)$$

where  $p_G$  refers to the probability that the global depolarising channel maps the state  $\rho$  to a maximally-mixed state, and  $I$  is the identity matrix.

The single-qubit state after the application of a local depolarising channel can be expressed using the Pauli matrices as [19]

$$\mathcal{E}_L(\rho) = (1 - \frac{3}{4}p'_L)\rho + \frac{p'_L}{4}(X\rho X + Y\rho Y + Z\rho Z) \quad (12)$$

Since  $p_G$  and  $p'_L$  represent depolarising noise probabilities, it is clear that they must have a value in the range  $[0, 1]$ .

The above expression can be rewritten by defining the parameter  $p_L = \frac{3}{4}p'_L$ , as

$$\mathcal{E}_L(\rho) = (1 - p_L)\rho + \frac{p_L}{3}(X\rho X + Y\rho Y + Z\rho Z) \quad (13)$$

where  $p_L \in [0, \frac{3}{4}]$ .

The single-qubit depolarising channel can also be described using the Kraus (operator-sum) representation:

$$\mathcal{E}(\rho) = \sum_{i=0}^3 K_i \rho K_i^\dagger \quad (14)$$

where the Kraus operators, for a single-qubit, are defined as:

$$K_0 = \sqrt{1-p}I, \quad K_1 = \sqrt{\frac{p}{3}}X, \quad K_2 = \sqrt{\frac{p}{3}}Y, \quad K_3 = \sqrt{\frac{p}{3}}Z \quad (15)$$

For the noiseless case, the channel reduces to the identity channel. At  $p = \frac{3}{4}$ , the channel becomes fully depolarising and applies single-qubit Pauli errors independently to each qubit. The output state can be thought of as a mixture of the original state and the maximally mixed state with some probability,  $p_L$ . The application of a fully depolarising channel results in the complete loss of information about the original state.

## 4 Linking Margins to Generalisation

In this section, we present empirical results demonstrating a strong correlation between geometric margins and generalisation performance.

Similar to the empirical results of Hur and Park [15] for QNNs, our results suggest that margins are a reliable indicator of generalisation performance for QSVMs, thereby providing a strong justification for margin-based generalisation analyses for QSVMs.

Taking inspiration from the systemic randomisation experiments performed in [14] and [15], we explore the effect of label corruption on test accuracy, which is used here as our proxy for generalisation performance. Additionally, we investigated the effect of corrupting increasing fractions of the labels in the training dataset on the geometric margin distribution across multiple datasets. The margin distribution was obtained by computing the distance of each sample to the separating hyperplane (the per-sample geometric margin).

This relationship was explored using four datasets, namely the High Time Resolution Universe Survey (South) (HTRU2) astrophysical dataset [32], a synthetic dataset describing a Gaussian distribution and the (White) Wine Quality and Heart Disease datasets. These datasets are further described in Appendix A.5.

Data from each of these datasets was encoded using IQP embedding [33]. This was implemented using a quantum circuit consisting of two qubits and one application of the unitary layer depicted in Figure 3.

The resulting density matrices were obtained from the circuit and used to calculate the elements of the kernel matrix using the Hilbert-Schmidt inner product  $(K(x_i, x_j) = \text{Tr}(\rho(x_i)\rho(x_j)))$ . This quantum kernel matrix was then used to train the classical SVM model from which we retrieved the geometric margin for each sample.

This experiment was conducted using 5-fold cross-validation (CV) [34] for reliability, with 250 samples for the HTRU2 dataset, 500 samples for the Gaussian dataset and 200 samples used for the Wine dataset. The entire Heart Disease dataset consisting of 303 samples was also used. Each dataset was preprocessed and scaled to the range  $[0, \pi]$  and transformed using principal component analysis (PCA) [35] such that the number of features in the dataset matched the number of qubits in the quantum circuit; a necessary condition for IQP encoding.

Figure 4 depicts boxplots for the various datasets showing the margin distribution for increasing fractions

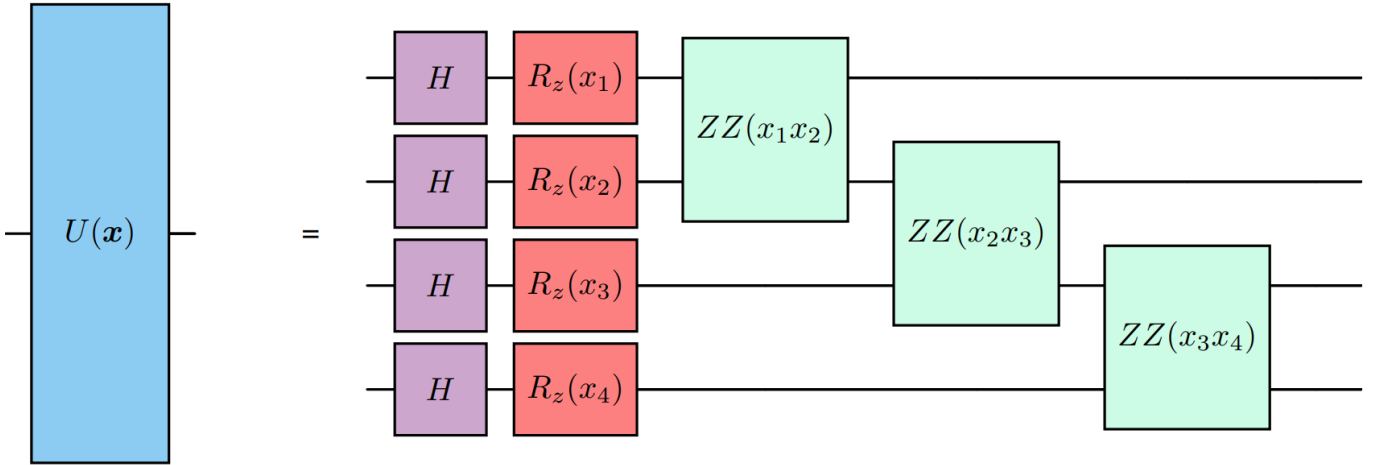


Figure 3: Quantum circuit layer implementing IQP encoding with nearest-neighbour entanglement using Hadamard gates (in purple),  $R_z$  rotations for each input feature  $x_i$  (in red) and ZZ entangling gates (in green).

of label corruption. These plots depict the margin distribution when no labels were corrupted (corruption fraction of 0), when half of the training dataset had flipped labels and when all training labels were flipped (corruption levels 0.5 and 1, respectively).

The plots become increasingly left-skewed as the fraction of corrupted labels increases. This can be observed since the median position of the margin distribution moves closer to more negative values as the level of corruption increases. For geometric margins, negative values are related to misclassifications of the QSVM model, which directly relates to poor generalisation performance.

We further analyse this relationship in Figure 5, where we now plot the test accuracy with the median geometric margin against increasing fractions of corrupted training labels. Here, the test accuracy was obtained from the average accuracy achieved using 5-fold CV, with the standard deviation used as the error. This plot was constructed for the above four datasets, and it can be seen that as corruption levels increase, the shapes of the accuracy and median geometric margin curves align almost completely (within the error bars). This is especially noted for the HTRU2 dataset.

Following this discovery, the linear relationship between the test accuracy and the median geometric margin, depicted in Figure 6, was explored. These plots de-

pict a strong correlation between the median geometric margin and test accuracy for all four datasets. Additionally, linear regression was performed for each dataset, and the Pearson correlation coefficient,  $r$ , was computed. This coefficient measures the linear correlation between two variables and is depicted for each dataset. The Pearson correlation coefficient can have values in the range  $[-1, 1]$ , with 1 (-1) being perfectly correlated variables with an increasing (decreasing) trend. A coefficient of 0 suggests no relationship between the involved variables. All datasets have Pearson coefficients greater than 0.9, with the HTRU2 dataset having the highest coefficient at  $r = 0.9987$ , suggesting an almost perfect correlation between the variables, despite clustering at extreme corruption levels.

## 5 Generalisation with Global and Local Depolarising Noise Models

In this section, we present numerical simulations establishing that global depolarising noise results in more optimistic generalisation performance for intermediate noise levels.

In order to fairly compare the effect of global and lo-

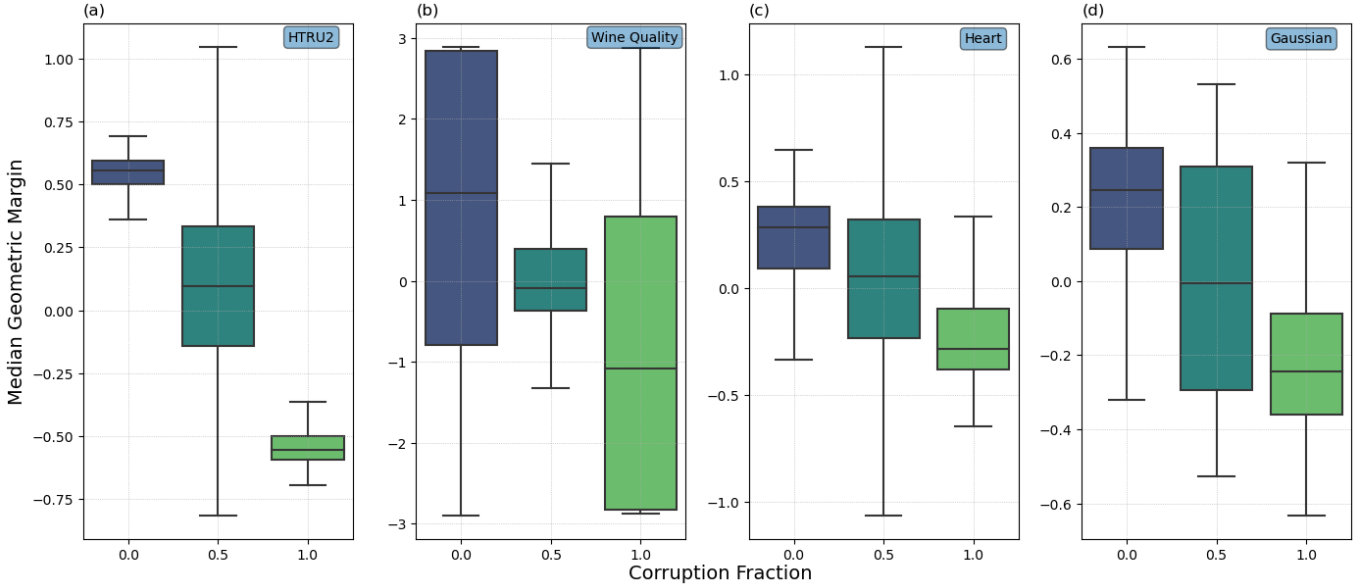


Figure 4: Box-plots depicting the geometric margin distribution calculated using datasets with increasing fractions of corrupted training labels for various datasets. Each dataset is labelled at the top-right corner of each plot. These plots were generated without the outliers to maintain the emphasis on the median geometric margin.

cal depolarising noise on a system of  $N$  qubits, we first equate their survival probabilities. The survival probability is the probability of an  $N$ -qubit state to remain unchanged after the application of a depolarising noise channel.

The survival probabilities can be easily seen from the definitions of the depolarising noise models in Section 3.3. From expression (11), it is clear that for  $N$  qubits, the survival probability for global depolarising noise,  $p_{GS}$ , is given by

$$p_{GS} = (1 - p_G) \quad (16)$$

From equations (13) and (14), it can be shown that for  $N$  qubits, the survival probability for local depolarising noise,  $p_{LS}$ , is expressed as

$$p_{LS} = (1 - p_L)^N \quad (17)$$

where  $p_G$  ( $p_L$ ) is the probability associated with global (local) depolarising channel over one encoding layer (qubit) and  $N$  is the number of qubits.

Adapting the above equations for  $L$  encoding layers requires the result by Du et al. [36]. This result demonstrates that a circuit with  $L$  layers of global depolarising channels applied after each unitary layer (depicted in Figure (8), is equivalent to the circuit portrayed in Figure 9 in which one noise channel is applied at the end of the circuit with the scaling  $p_{GE} = 1 - (1 - p_G)^L$ .

From the above result, for  $L$  unitary layers, equations (16) and (17) become  $p_{GS} = (1 - p_{GE})$  and  $p_{LS} = (1 - p_L)^{NL}$ , respectively.

Numerical simulations comparing test accuracy for increasing global and local depolarising noise levels using these definitions were then performed across various datasets.

Henceforth, the terms local (global) test accuracy will be used to describe the accuracy obtained from the QSVM model trained using quantum kernel values obtained from a quantum circuit with local (global) depolarising noise channels. Additionally, since only depolarising noise is discussed here; local and global noise will be used instead, for brevity.

The methodology to obtain the local test accuracy fol-

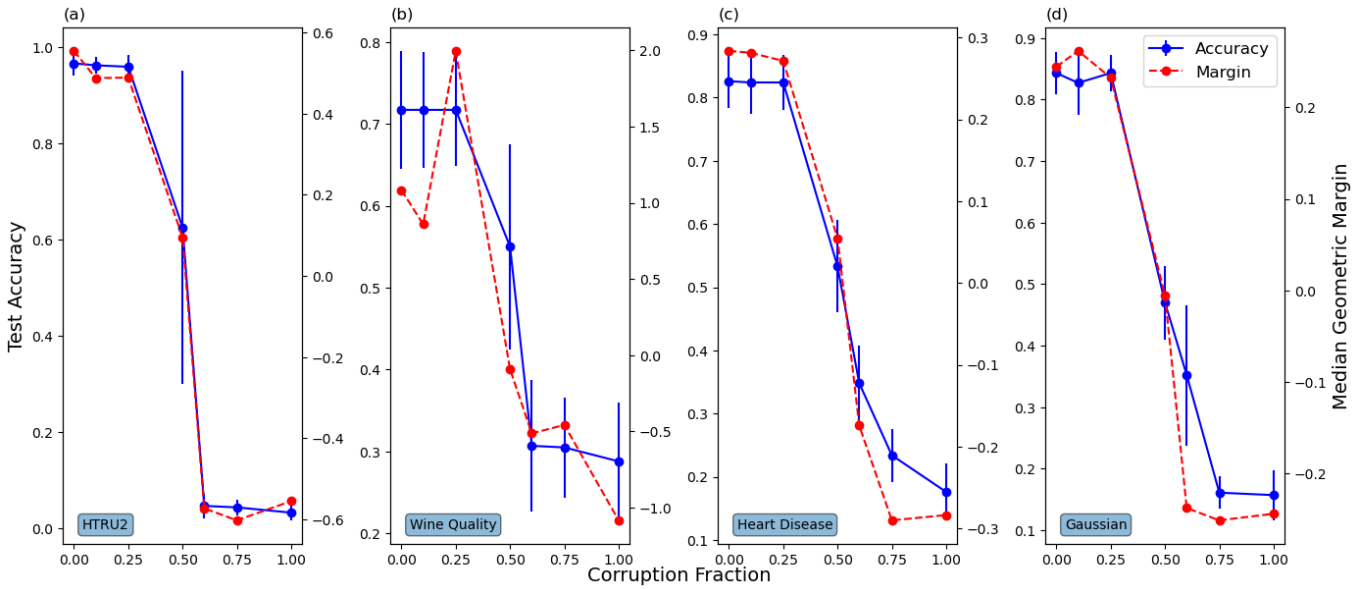


Figure 5: Plots overlaying the decreasing test accuracy and median geometric margin graphs for increasing fractions of corrupted training labels. The test accuracy (blue) is depicted with the error obtained from 5-fold CV, and the geometric margins (red) are taken from the box-plots in Figure 4 above. Each dataset is labelled at the bottom-left corner of each plot.

lows similarly as described in Section 4, with the quantum circuit described by Figure 7. This circuit depicts local depolarising noise channels applied to each qubit after each unitary layer, following the experimental setup used in [17].

We first matched the survival probabilities of the noise models following the above discussion. Thereafter, we obtained the resulting density matrix from the ideal quantum circuit. The density matrix affected by global depolarising noise was computed using equation (11). This density matrix is then used to calculate the quantum kernel element, which will, in a similar manner, yield the global test accuracy.

Figure 10 portrays the difference in the test accuracy obtained when using the global and local noise models, respectively. A dual axis is displayed, with one axis representing increasing levels of local depolarising noise, and the other showing the equivalent global depolarising noise level as a result of their matched survival probabilities. This simulation was performed for two datasets: the Wine Quality and Heart Disease

datasets. The Wine Quality dataset was analysed using 1000 samples, with two and three qubits, respectively. The Heart Disease dataset was analysed using two qubits and 303 samples. The average accuracies obtained after implementing 5-fold CV were used to construct the plot. The shaded region in the plots represent the uncertainty. These values were calculated using the standard formula to calculate the uncertainty of the quantity  $A - B$  as  $\sigma_E = \sqrt{\sigma_A^2 + \sigma_B^2}$ , where  $\sigma_A$  and  $\sigma_B$  are the standard deviations of the respective quantities. In this case,  $A$  and  $B$  represent the accuracy from the global and local noise setups, respectively. With this formula, the standard deviations were used to obtain the uncertainty values for the test accuracy of each noise probability.

Figure 10 clearly shows a positive difference in test accuracy for each of the plots in the intermediate local depolarising noise range. This corresponds to a larger test accuracy from the global noise simulation compared to the local noise simulation. This clearly suggests that global depolarising noise yields more op-

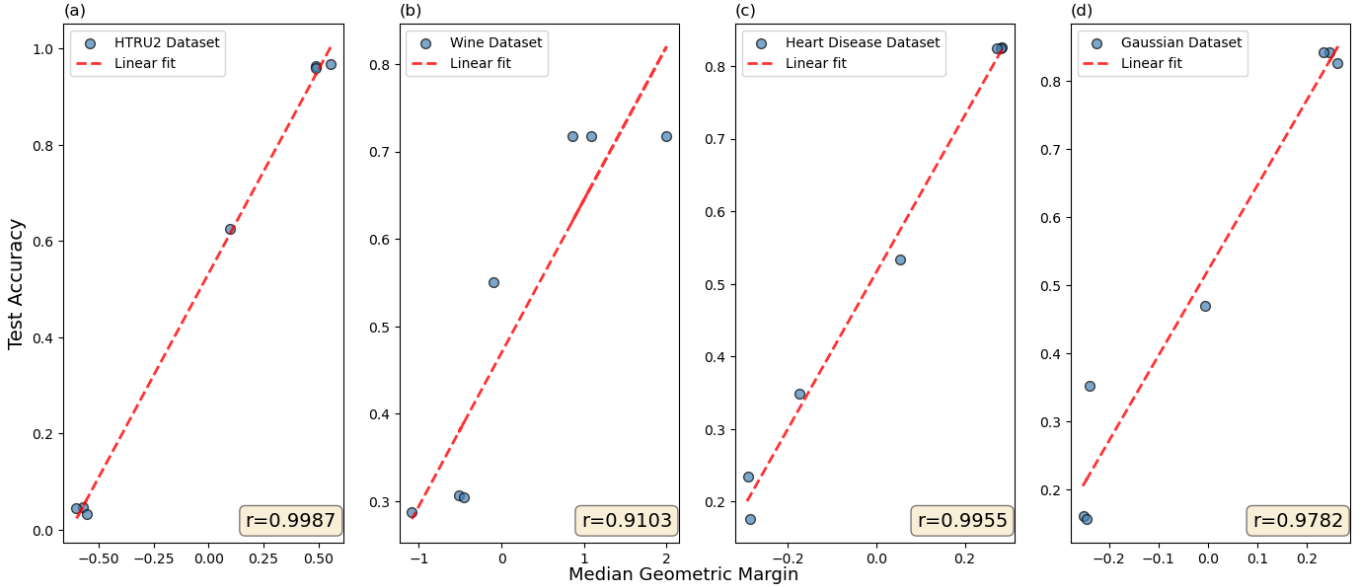


Figure 6: Plots depicted the linear correlation between test accuracy and median geometric margin. Linear regression was performed, and the Pearson correlation coefficient is depicted at the bottom-right for each dataset. The linear fit for each dataset is depicted by the dashed red line.

timistic results in the form of higher test accuracy than local noise. This is because global depolarising noise does not capture the impact of errors on individual qubits but on the system as a whole. Additionally, this approach does not model the degradation of the QSVM model performance as accurately as the local noise simulation in the intermediate noise range.

For the Wine Quality plot with two qubits and the Heart Disease plot, the increase appears noticeably from the local noise level of 0.1 to 0.5 and 0.6, respectively. Afterwards, the noise becomes too high, and the performance of both models degrades to the same degree. A sharper rise is noted from zero noise for the wine quality plot with three qubits compared to the other two plots. This indicates that the local noise impact is more substantial due to errors introduced by the additional qubit, resulting in a difference in performance for relatively low local noise levels. This figure provides empirical motivation for the study of local depolarising noise over global noise since it is more realistic when capturing noise faced by current NISQ hardware.

## 6 Results

### 6.1 Kernel Bounds

In this section, we present bounds for the case of kernel elements affected by a single application of a local depolarising noise channel for an  $N$ -qubit system. Bounds considering  $L$  applications of the local depolarising noise channel are presented in Appendix A.1.

Based on the definitions in Section 3, we use the tensor product of the single qubit local depolarising noise channel,  $(\mathcal{E}_L^{\otimes N} = \mathcal{E}_L \otimes \mathcal{E}_L \otimes \dots \otimes \mathcal{E}_L)$  to express the resulting state after individually applying a local depolarising channel on each qubit in an  $N$ -qubit system as:

$$\tilde{\rho} = \mathcal{E}(\rho) = \sum_{\mathbf{m} \in \{0,1,2,3\}^N} \left( \bigotimes_{k=1}^N K_{m_k} \right) \rho \left( \bigotimes_{k=1}^N K_{m_k}^\dagger \right) \quad (18)$$

where  $\mathbf{m} = \{m_1, m_2, \dots, m_N\}$  is the multi-index for all possible combinations of the Kraus operators defined

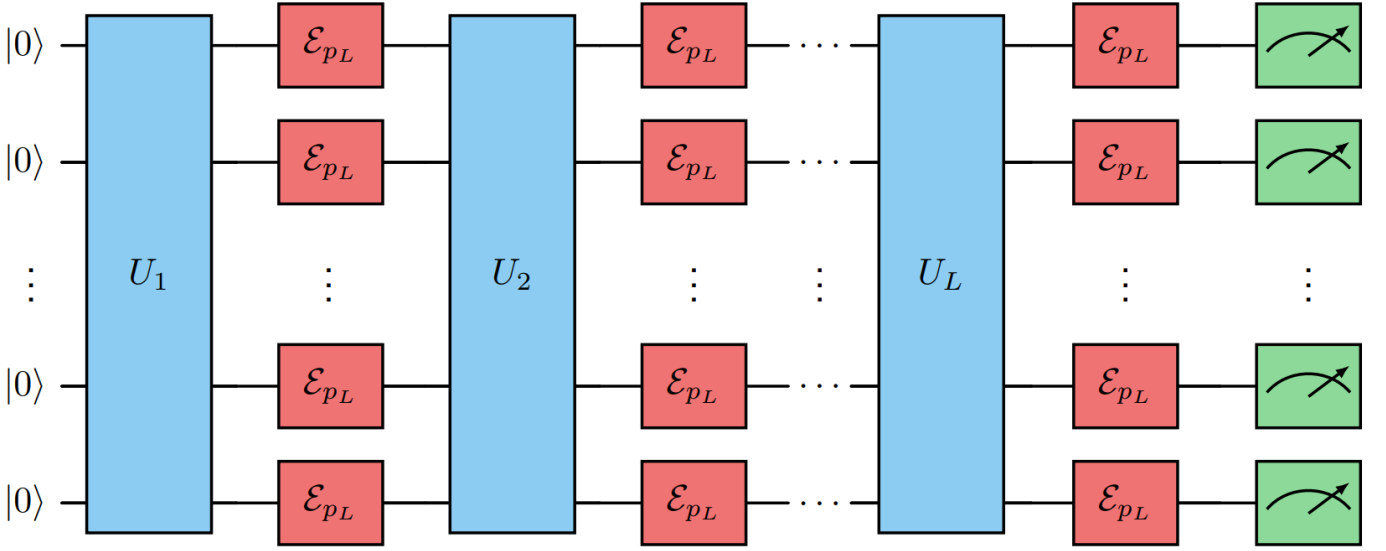


Figure 7: Quantum circuit used to implement local depolarising noise channels for  $N$  qubits with  $L$  unitary encoding layers (blue) followed by a layer of local depolarising noise channels (red).

by the expressions in (15) with  $m_k \in [0, 3]$  for each qubit  $k$ .

This can be written explicitly as:

$$\tilde{\rho} = \sum_{m_1, \dots, m_N=0}^3 (K_{m_1} \otimes \dots \otimes K_{m_N}) \rho (K_{m_1}^\dagger \otimes \dots \otimes K_{m_N}^\dagger)$$

For some kernel matrix of size  $n \times n$ , we first bound the ratio of the  $ij$ -th noisy kernel element with its corresponding noiseless element.

Using the kernel definition, we get the relative expression:

$$\frac{\tilde{K}_{ij}}{K_{ij}} = \frac{\text{Tr}(\tilde{\rho}_i \tilde{\rho}_j)}{\text{Tr}(\rho_i \rho_j)} \quad (19)$$

where  $\tilde{\rho}_i$  represents the noisy density matrix representing the state after the application of the noisy depolarising channel.

Now, we substitute the expression for the noisy density matrix and using the linearity property of the trace operator. Additionally, we use the cyclic properties of the trace operator and note that the Kraus operators defined in expression 15 are Hermitian ( $K = K^\dagger$ ), due to the Pauli matrices also being Hermitian to obtain:

$$\frac{\tilde{K}_{ij}}{K_{ij}} = (1 - p)^{2N} + \frac{1}{\text{Tr}(\rho_i \rho_j)} \sum_{\substack{\mathbf{m}, \mathbf{n} \in \{0, 1, 2, 3\}^N \\ (\mathbf{m}, \mathbf{n} \neq 0)}} \text{Tr} \left( \rho_i \left( \bigotimes_{k=1}^N K_{m_k} K_{n_k} \right) \rho_j \left( \bigotimes_{k=1}^N K_{n_k} K_{m_k} \right) \right) \quad (20)$$

The first term is as a result of separating the  $\mathbf{m} = \mathbf{n} = 0$  term from the rest of the sum and substituting the definition of the Kraus operator,  $K_0$ .

From this equation, we note that the first term is the probability of the kernel element remaining unchanged after the application of the noise channel, while the second term is the contribution due to noise.

Now, we bound the noisy contribution, defined by  $\tilde{N}$ , and write it in the form

$$\tilde{N} = \frac{1}{\text{Tr}(\rho_i \rho_j)} \sum_{\substack{\mathbf{m}, \mathbf{n} \in \{0, 1, 2, 3\}^N \\ (\mathbf{m}, \mathbf{n} \neq 0)}} \text{Tr} (\rho_i Q_{mn} \rho_j Q_{nm}) \quad (21)$$

where, we define

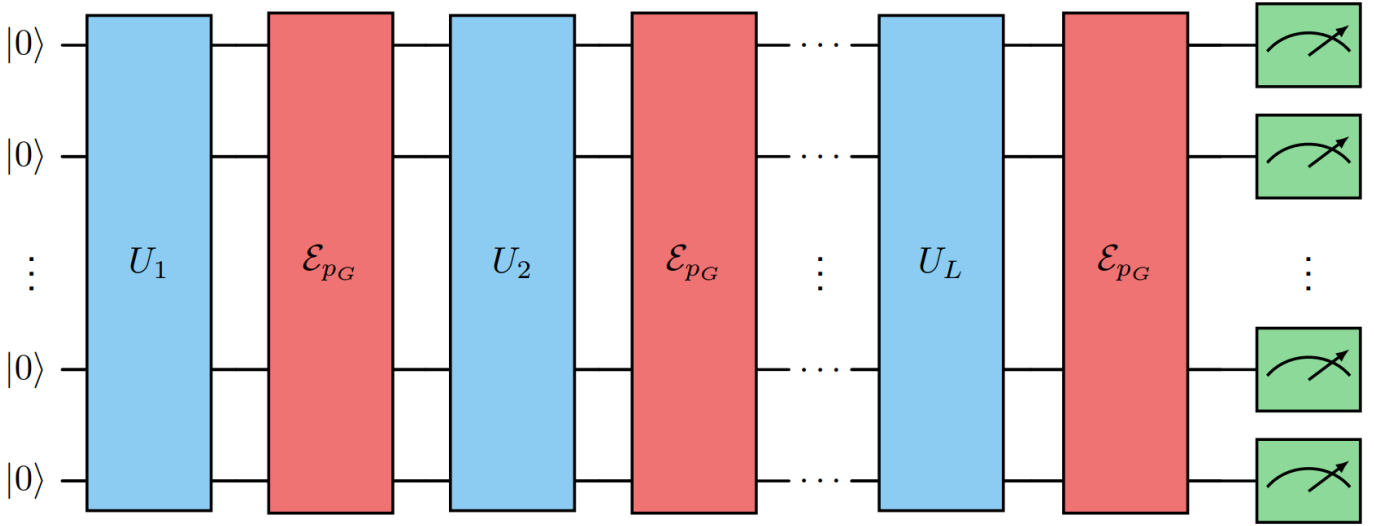


Figure 8: Quantum circuit used to implement global depolarising noise channels for  $N$  qubits with  $L$  unitary encoding layers (blue) followed by a layer of global depolarising noise channels (red).

$$Q_{mn} = \bigotimes_{k=1}^N (K_{m_k} K_{n_k}) \quad (22)$$

Now, we note that for some  $\alpha, \beta \in \{0, 1, 2, 3\}$ ,

$$K_\alpha K_\beta = c_\alpha c_\beta \sigma_\alpha \sigma_\beta = c_{\alpha\beta} \sigma_\alpha \sigma_\beta$$

We define the piecewise function for the constants  $c_{\alpha\beta} = c_\alpha c_\beta$  using the Kraus operator coefficients as:

$$c_{\alpha\beta} = \begin{cases} (1-p) & \text{if } \alpha = \beta = 0 \\ \sqrt{\frac{p}{3}(1-p)} & \text{if } \alpha = 0, \beta = i \text{ or } \alpha = i, \beta = 0 \\ \frac{p}{3} & \text{if } \alpha \text{ and } \beta \in i \end{cases}$$

where  $i \in \{1, 2, 3\}$ .

From this, it is clear that we find that:

$$Q_{mn} = \prod_{k=1}^N c_{m_k n_k} \bigotimes_{k=1}^N (\sigma_{m_k} \sigma_{n_k}) = Q_{nm}^\dagger \quad (23)$$

Hence, the noisy term can be rewritten as:

$$\tilde{N} = \sum_{\substack{\mathbf{m}, \mathbf{n} \in \{0, 1, 2, 3\}^N \\ (\mathbf{m}, \mathbf{n} \neq 0)}} \left( \prod_{k=1}^N (c_{m_k n_k})^2 \right) \frac{1}{\text{Tr}(\rho_i \rho_j)} \text{Tr} \left( \rho_i \left( \bigotimes_{k=1}^N \sigma_{m_k} \sigma_{n_k} \right) \rho_j \left( \bigotimes_{k=1}^N \sigma_{n_k} \sigma_{m_k} \right) \right) \quad (24)$$

Using the trace inequalities, we can bound the trace term as:

$$\text{Tr} \left( \rho_i \left( \bigotimes_{k=1}^N \sigma_{m_k} \sigma_{n_k} \right) \rho_j \left( \bigotimes_{k=1}^N \sigma_{n_k} \sigma_{m_k} \right) \right) \leq \left\| \left( \rho_i \left( \bigotimes_{k=1}^N \sigma_{m_k} \sigma_{n_k} \right) \rho_j \left( \bigotimes_{k=1}^N \sigma_{n_k} \sigma_{m_k} \right) \right) \right\|_1 \quad (25)$$

Using Hölders inequality for the Schatten norm, where  $\|AB\|_1 \leq \|A\|_p \|B\|_q$  such that  $\frac{1}{p} + \frac{1}{q} = 1$ , with  $p = q = 2$ , we get

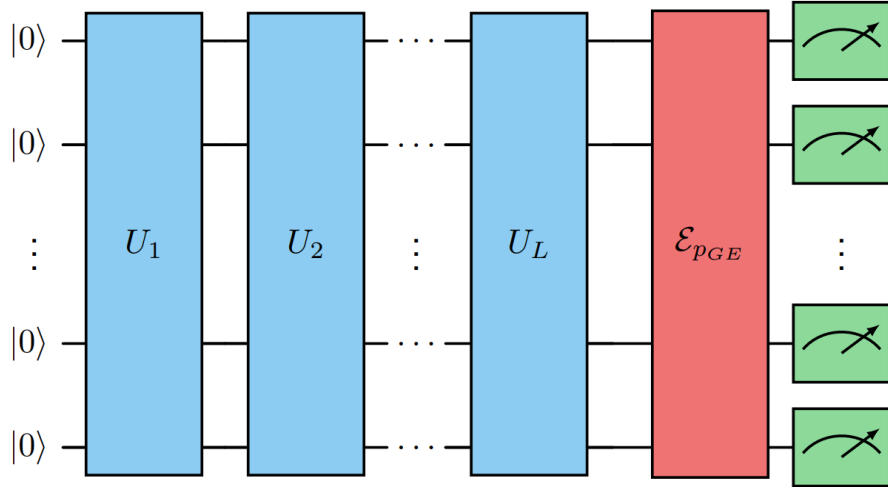


Figure 9: Equivalent quantum circuit used to implement global depolarising noise channels for  $N$  qubits with  $L$  unitary encoding layers (blue) followed by one layer of global depolarising noise channels (red) at the end of the circuit with a scaled global noise value. The scaling used corresponds to  $p_{GE} = 1 - (1 - p_G)^L$ , where  $p_G$  is the global noise value used per noise layer in Figure 8.

$$\left\| \left( \rho_i \left( \bigotimes_{k=1}^N \sigma_{m_k} \sigma_{n_k} \right) \rho_j \left( \bigotimes_{k=1}^N \sigma_{n_k} \sigma_{m_k} \right) \right) \right\|_1 \leq \|\rho_i\|_2 \left\| \left( \bigotimes_{k=1}^N \sigma_{m_k} \sigma_{n_k} \right) \rho_j \left( \bigotimes_{k=1}^N \sigma_{n_k} \sigma_{m_k} \right) \right\|_2 \quad (26)$$

Now, noting that since  $U = \bigotimes_{k=1}^N \sigma_{m_k} \sigma_{n_k}$  and  $V = \bigotimes_{k=1}^N \sigma_{n_k} \sigma_{m_k}$  are unitary matrices, we can rewrite this using the unitarily invariant property of Schatten norms, as

$$\|\rho_i\|_2 \left\| \left( \bigotimes_{k=1}^N \sigma_{m_k} \sigma_{n_k} \right) \rho_j \left( \bigotimes_{k=1}^N \sigma_{n_k} \sigma_{m_k} \right) \right\|_2 = \|\rho_i\|_2 \|\rho_j\|_2 \quad (27)$$

By employing the definition of the  $p$ -Schatten norm ( $\|A\|_p = [\text{Tr}(|A|^p)]^{1/p}$ ) and the Hermitian property of unitary matrices, we can write this as

$$\begin{aligned} \|\rho_i\|_2 \|\rho_j\|_2 &= \sqrt{(\text{Tr}|\rho_i|^2)} \sqrt{(\text{Tr}|\rho_j|^2)} \\ &= \sqrt{(\text{Tr}|\rho_i|^2)(\text{Tr}|\rho_j|^2)} \\ &= \sqrt{\text{Tr}(\rho_i^2) \text{Tr}(\rho_j^2)} \end{aligned} \quad (28)$$

Finally, for some density matrix,  $\rho$ , we have the relation

$$\frac{1}{2^N} \leq \text{Purity} = \text{Tr}(\rho^2) \leq 1$$

Using this, we bound the term as follows:

$$\|\rho_i\|_2 \|\rho_j\|_2 = \sqrt{\text{Tr}(\rho_i^2) \text{Tr}(\rho_j^2)} \leq 1 \quad (29)$$

Hence, the noisy contribution becomes

$$\tilde{N} \leq \sum_{\substack{\mathbf{m}, \mathbf{n} \in \{0,1,2,3\}^N \\ (\mathbf{m}, \mathbf{n} \neq 0)}} \left( \prod_{k=1}^N (c_{m_k n_k})^2 \right) \frac{1}{K_{ij}} \quad (30)$$

Thus, the value of the  $ij$ -th kernel element in the kernel matrix is bounded by

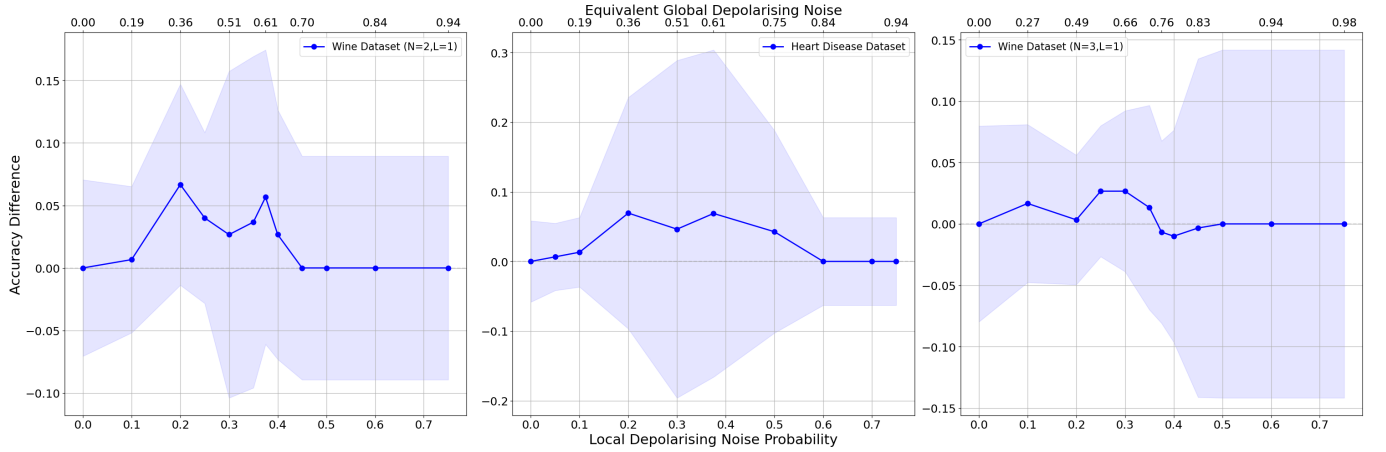


Figure 10: Plots depicting the difference in the test accuracy obtained when using the global and local depolarising noise models. The accuracy difference is shown for varying levels of local noise. The equivalent global noise is depicted for selected local noise levels using dual  $x$ -axes for readability. The shaded blue region depicts the uncertainty. The values,  $N$  and  $L$ , for the Wine dataset indicate the differing number of qubits and unitary layers used in the quantum circuit, respectively. The Heart Disease dataset used two qubits with one unitary layer.

## 6.2 Upper Bounds (Soft Margin)

$$\tilde{K}_{ij} \leq (1-p)^{2N} K_{ij} + \sum_{\substack{\mathbf{m}, \mathbf{n} \in \{0,1,2,3\}^N \\ (\mathbf{m}, \mathbf{n} \neq 0)}} \left( \prod_{k=1}^N (c_{m_k n_k})^2 \right) \quad (31)$$

Here, it is clear to see that the first term describes the kernel element remaining unchanged with some probability, and the second term describes some error that will alter the kernel elements due to noise with some probability. Due to the normalisation condition (where all probabilities must sum to 1), we can simply rewrite the above as:

$$\tilde{K}_{ij} \leq (1-p)^{2N} K_{ij} + (1 - (1-p)^{2N}) \quad (32)$$

This upper-bounds the resulting kernel element after the local application of a depolarising noise channel.

The resulting kernel element after  $L$  local applications of the depolarising channel can be bound using a similar structure. This proof is shown in Appendix A.1 as:

$$\tilde{K}_{ij} \leq (1-p)^{2LN} K_{ij} + (1 - (1-p)^{2LN}) \quad (33)$$

In this section, we present the upper bounds for the geometric margin affected by local depolarising noise for  $L = 1$ . These bounds can easily be modified for  $L$  unitary layers by simply using the factor  $(1-p)^{2LN}$  instead of  $(1-p)^{2N}$ , as depicted in expression (33).

The following bounds are constructed using optimality relations associated with the dual objective functions. We begin by comparing two dual objective functions; the first, a function of the kernel affected by noise, along with the corresponding optimal noisy solution, and the second, a function of the noisy kernel but another non-optimal dual solution. In particular, we choose the dual solution optimised for the noiseless kernel. By optimality relations, we get the following relation in this case:

$$\mathcal{L}(\alpha, \tilde{K}) \leq \mathcal{L}(\tilde{\alpha}, \tilde{K}) \quad (34)$$

$$\sum_{i=1}^m \alpha_i - \frac{1}{2} \sum_{i,j=1}^m \alpha_i \alpha_j y_i y_j \tilde{K}_{ij} \leq \sum_{i=1}^m \tilde{\alpha}_i - \frac{1}{2} \sum_{i,j=1}^m \tilde{\alpha}_i \tilde{\alpha}_j y_i y_j \tilde{K}_{ij} \quad (35)$$

The RHS of this inequality can be rewritten with absolute values since Lagrangian variables are defined to be

non-negative. We can then write this in terms of the L1-norm.

$$\|\alpha\|_1 - \frac{1}{2}\|\tilde{w}\|_\alpha^2 \leq \|\tilde{\alpha}\|_1 - \frac{1}{2}\|\tilde{w}\|_{\tilde{\alpha}}^2 \quad (36)$$

Rearranging this gives the form:

$$\|\tilde{w}\|_{\tilde{\alpha}}^2 - \|\tilde{w}\|_\alpha^2 \leq 2\|\tilde{\alpha}\|_1 - 2\|\alpha\|_1 \quad (37)$$

We now observe the following results for the soft-margin case:

$$\|\tilde{\alpha}\|_1 = \|\tilde{w}\|_{\tilde{\alpha}}^2 + C \sum_{i=1}^m \xi_i \quad (38)$$

$$C \sum_{i=1}^m \xi_i^* \leq mC \quad (39)$$

We can now combine these results, which are proven as Results 1 and 2 respectively in Appendix A.3 to bound the first term of the RHS as  $2\|\tilde{\alpha}\|_1 \leq 2\|\tilde{w}\|_{\tilde{\alpha}}^2 + 2mC$ .

We can similarly use the inequality from Result 1 in Appendix A.3 ( $\|w\|_\alpha^2 \leq \|\alpha\|_1$ ) to bound the second term of the RHS.

Using the above inequalities, the RHS of equation (37) can be written as

$$\|\tilde{w}\|_{\tilde{\alpha}}^2 - \|\tilde{w}\|_\alpha^2 \leq 2\|\tilde{w}\|_{\tilde{\alpha}}^2 + 2mC - 2\|w\|_\alpha^2 \quad (40)$$

Applying Results 1A and 1B (equations (88) and (90) respectively), proven in Appendix (A.3) results in:

$$2\|w\|_\alpha^2 - 2mC \leq (1-p)^{2N} (\|w\|_{\tilde{\alpha}}^2 + \|w\|_\alpha^2) \quad (41)$$

We now re-formulate the bound in terms of the margins. For brevity, we will refer to the margin obtained from the SVM trained on a quantum circuit with no noise as the clean margin, and that obtained from a quantum circuit with (local depolarising) noise as the noisy margin. Additionally, when we discuss the noisy margin, we exclusively refer to the geometric margin obtained from the SVM model that has been trained with a kernel matrix obtained from a noisy quantum circuit, but has been evaluated with reference to the ideal kernel matrix.

Finally, we arrive at the upper bound for the noisy margin for the case of non-separable data.

$$\gamma_{\tilde{\alpha}}^2 \leq \frac{(1-p)^{2N}}{2(1-mC\gamma_\alpha^2) - (1-p)^{2N}} \gamma_\alpha^2 \quad (42)$$

The margin upper bounds for the separable (hard margin) case can be derived through a similar/analogue procedure to achieve the bounds:

$$\gamma_{\tilde{\alpha}}^2 \leq \frac{(1-p)^{2N}}{(2 - (1-p)^{2N})} \gamma_\alpha^2 \quad (43)$$

We can clearly see that the soft-margin bounds reduce to the hard-margin bounds when  $C = 0$  as expected.

Additionally, considering that  $(1-p)^{2N} \leq 2$ , which follows from  $0 \leq (1-p)^{2N} \leq 1$ , it can be verified that the upper bound of the squared noisy margin is always non-negative, as expected.

Testing the extreme cases of this bound gives us the following relations. For  $p = 0$ , the bound reduces to the clean margin at zero noise and holds as an equality:

$$\gamma_\alpha^2 = \gamma_{\tilde{\alpha}}^2$$

This is expected for the scenario with no noise.

At maximum noise, which is  $\frac{3}{4}$  due to the parametrisation discussed in Section 3, ( $p = p'_L = \frac{3}{4}p_L$ ) the bound simplifies to

$$\frac{(0.25)^{2N}}{2 - (0.25)^{2N}} \gamma_\alpha^2 \geq \gamma_{\tilde{\alpha}}^2 \quad (44)$$

Additionally, to ensure the validity of the bounds, we must impose the following constraints. Two necessary condition must be that the denominator must not be 0 and that the bound must be non-negative to be valid.

Since the numerator is always non-negative, we just impose that the denominator also be non-negative:

$$2(1-mC\gamma_\alpha^2) - (1-p)^{2N} > 0$$

Finally, we get:

$$mC\gamma_\alpha^2 < \frac{2 - (1-p)^{2N}}{2} \quad (45)$$

This constraint gives us an upper bound for the acceptable values of  $mC\gamma_\alpha^2$

Thus we can define,

$$C'_{\max} := \frac{2 - (1-p)^{2N}}{2\gamma_\alpha^2} \quad (46)$$

where we defined a training sample size dependent regularisation parameter  $C' = mC$  for simplicity.

Now, in attempt to find a minimum  $C'$  value, we rearrange the bound in terms of  $C'$  to get:

$$\frac{1}{\gamma_\alpha^2} - \frac{((1-p)^{2N})(\gamma_{\tilde{\alpha}}^2 + \gamma_\alpha^2)}{2\gamma_\alpha^2\gamma_{\tilde{\alpha}}^2} \leq C'_{\min} \quad (47)$$

For the bound to be valid,  $C'$  must be at least the LHS. Thus, we impose the equality to get:

$$\frac{2 - (1-p)^{2N}}{2\gamma_\alpha^2} - \frac{(1-p)^{2N}}{2\gamma_{\tilde{\alpha}}^2} = C'_{\min} \quad (48)$$

This can be rewritten as:

$$C'_{\max} - \frac{(1-p)^{2N}}{2\gamma_{\tilde{\alpha}}^2} = C'_{\min} \quad (49)$$

It is clear here that  $C'_{\min} \leq C'_{\max}$ . For the bound to be valid,  $C'$  must satisfy:

$$C'_{\min} \leq C' < C'_{\max}$$

Interestingly, the expression for the minimum  $C'$  value contains the noisy margin, i.e. the quantity that we want to bound. We explore two avenues in which to side-step this issue, since the true noisy margin value is considered to be unknown.

In the first option, we find an upper bound for  $C'_{\min}$  by using the trivial bound  $\gamma_{\tilde{\alpha}}^2 \leq \gamma_\alpha^2$  to upper bound  $C'_{\min}$ .

Here, we get:

$$C'_{\min} \leq \frac{1 - (1-p)^{2N}}{\gamma_\alpha^2} \quad (50)$$

However, we should note that this bound on  $C'_{\min}$  becomes looser as  $p$  increases.

The second option involves using a separate validation set when conducting numerical experiments to estimate the value of the noisy margin. This option will be explored in greater detail in Section 7.

### 6.3 Lower Bounds (Soft Margin)

Here, we present lower bounds for the noisy margin derived using optimality relations for primal objective functions.

Due to optimality, the primal objective function evaluated at the optimal noiseless solution must be at most any other feasible solution, such as the noisy solution evaluated at this primal objective function.

From this, it can be seen that

$$P(\mathbf{w}_\alpha, b, \xi) \leq P(\mathbf{w}_{\tilde{\alpha}}, \tilde{b}, \zeta) \quad (51)$$

where  $\zeta, \xi$  represents the slack variables for the noiseless optimisation problem with noisy and noiseless dual solutions, respectively.

$$\frac{1}{2}\|\mathbf{w}\|_\alpha^2 + C \sum_{i=1}^m \xi_i \leq \frac{1}{2}\|\mathbf{w}\|_{\tilde{\alpha}}^2 + C \sum_{i=1}^m \zeta_i \quad (52)$$

Since  $\frac{1}{2}\|\mathbf{w}\|_\alpha^2 \leq \frac{1}{2}\|\mathbf{w}\|_{\tilde{\alpha}}^2 + C \sum_{i=1}^m \xi_i$ , we get

$$\frac{1}{2}\|\mathbf{w}\|_\alpha^2 \leq \frac{1}{2}\|\mathbf{w}\|_{\tilde{\alpha}}^2 + C \sum_{i=1}^m \zeta_i \quad (53)$$

Applying the result  $C \sum_{i=1}^m \zeta_i = \|\tilde{\mathbf{w}}\|_{\tilde{\alpha}}^2 - \|\mathbf{w}\|_{\tilde{\alpha}}^2 + C \sum_{i=1}^m \tilde{\xi}_i$  which is proven in Appendix A.4 gives:

$$\frac{1}{2}\|\mathbf{w}\|_\alpha^2 \leq \frac{1}{2}\|\mathbf{w}\|_{\tilde{\alpha}}^2 + \|\tilde{\mathbf{w}}\|_{\tilde{\alpha}}^2 - \|\mathbf{w}\|_{\tilde{\alpha}}^2 + C \sum_{i=1}^m \tilde{\xi}_i \quad (54)$$

Applying results 1A (88) and 3 (104) respectively gives

$$\|\mathbf{w}\|_{\tilde{\alpha}}^2 \leq \frac{Cm - \frac{1}{2}\|\mathbf{w}\|_\alpha^2}{\left(\frac{1}{2} - (1-p)^{2N}\right)} \quad (55)$$

Formulating this in terms of the margin gives:

$$\gamma_{\tilde{\alpha}}^2 \geq \frac{\gamma_\alpha^2(1 - 2(1-p)^{2N})}{2Cm\gamma_\alpha^2 - 1} \quad (56)$$

Similar to the upper bound, to ensure the validity of this bound, we must ensure that the following conditions be imposed.

Firstly, the denominator must be non-zero, which gives the constraint:

$$\gamma_\alpha^2 Cm \neq \frac{1}{2} \quad (57)$$

Secondly, we impose that the bound itself be non-negative to ensure that it is non-trivial, by imposing that the numerator and denominator be the same sign. This

means that we have 2 cases; one where both the numerator and denominator are positive and one in which both are negative, i.e:

$$\frac{1}{2} \geq (1-p)^{2N} \text{ and } \gamma_\alpha^2 C m > \frac{1}{2} \quad (58)$$

or

$$\frac{1}{2} \leq (1-p)^{2N} \text{ and } \gamma_\alpha^2 C m < \frac{1}{2} \quad (59)$$

For valid, non-trivial bounds, one of the two following conditions must hold.

$$(1-p)^{2N} \leq \frac{1}{2} < \gamma_\alpha^2 C m \quad (60)$$

or

$$\gamma_\alpha^2 C m < \frac{1}{2} \leq (1-p)^{2N} \quad (61)$$

In the case where both the numerator and denominator of the bound are positive, we rearranging the bound in terms of  $C' = mC$  to get:

$$C' \geq \frac{1 - 2(1-p)^{2N}}{2\gamma_\alpha^2} + \frac{1}{2\gamma_\alpha^2} \quad (62)$$

where  $1 - 2(1-p)^{2N} \geq 0$  from the above constraints.

Similarly, we can define  $C'_{\min}$  using the equality and upper-bound this quantity using a validation set during numerical runs.

## 7 Numerical Experiments

### 7.1 Dataset Selection

The upper and lower bounds naturally give us a restriction on the feasible values of the regularisation parameter,  $C$ . However, it should be noted that these feasible values depend on the noise level parameter,  $p$ . In other words, the feasible range changes for different values of  $p$ .

In order to fairly test the upper margin bounds for increasing  $p$ , we must choose a  $C'$  value that satisfies

the above constraints simultaneously for all noise values. To do this, we must use datasets with an overlap in the range for  $C'$  values that satisfy the above constraints for each noise level. Not all datasets are guaranteed to have this overlapping feasible range, and so we use a dataset selection pipeline in order to find feasible datasets for our numerical tests.

In order to implement this pipeline, we first note that the value of the clean margin  $\gamma_\alpha^2$  used to calculate the  $C'_{\min}$  and  $C'_{\max}$  values depends on the initial regularisation parameter,  $C_0$  used to train the SVM model on a Gram matrix obtained with an ideal quantum circuit.

In practice, this  $C_0$  value is chosen among a range of values using 5-fold CV, keeping accuracy and model performance in mind. The selected initial parameter was then used to obtain the value of the clean margin. This clean margin is then used to compute the minimum and maximum allowed  $C'$  value. A particular dataset was selected if a range of acceptable  $C'$  values was detected. In the case where no overlap was found, that particular dataset was rejected.

However, we stress that this is specifically for the fair comparison of the margin values at different noise levels. If one were to test the margin bounds at some specific noise level, there would be no need to search for overlapping ranges. The bounds would be valid for that particular feasible range of  $C'$  values.

An important caveat that should be noted about the calculation of the minimum  $C'$  value, as discussed in Section 6, is that the expression includes the noisy margin. Since this is the value that we want to bound, it is obviously assumed to be unknown. As discussed above, the exact  $C'_{\min}$  value can be trivially bounded. However, this results in a loose upper-bound for large noise values. In our numerical experiments, a closer estimate for the value of  $C'_{\min}$  is obtained by computing an estimate noisy margin on a separate, held-out validation set. This value is used in the  $C'_{\min}$  calculation and consistently provides a tighter estimate of the minimum value. Thus, for this pipeline, the data is split into training and validation datasets.

At this stage we adopt different definitions for the regularisation parameter used to train the model and the one present in the bounds. In the interest of keeping our SVM model consistent for fair comparison across noise levels, we keep the regularisation parameter used

to train the SVM as  $C_0$ .

We then define the theoretical regularisation parameter used in the bounds to differ from the practical parameter by a scaling factor. A similar scaling strategy is discussed in [37]. In particular, these parameters are related as:

$$C = \frac{C_0}{m^\beta} \quad (63)$$

where  $\beta$ , is a tunable parameter used to control how strongly  $C$  depends on  $m$ . This parameter is introduced to allow for flexibility in choosing the scaling to align with the constraints of the theoretical parameter,  $C'$  defined above. For our re-parametrisation,  $C' = Cm$ , this becomes  $C' = C_0 m^{1-\beta}$ . This value represents the theoretical value for which our upper margin bounds are not violated when tested on a model trained using regularisation parameter,  $C_0$ .

Once feasible datasets are selected, an appropriately scaled  $C'$  value is selected from the available feasible range to conduct numerical experiments.

## 7.2 Validating the Margin Bounds

Table 1: The number of unitary layers and samples are depicted along with the initial regularisation parameter, with the dataset split and the feasible  $C'$  range used to test the upper margin bounds.

Dataset	Layers	$C_0$	Samples	Data Split	Feasible $C'$ Range
Heart Disease	1	10	303	75/25	[0,21.1)
Gaussian	2	100	500	75/25	[32.4,112.6)
Breast Cancer	1	1000	569	80/20	[0,544.7)
Wine	1	1000	350	80/20	[0,38.9)
Wine	2	1000	400	80/20	[0.6, 125)

We outline the pipeline followed to numerically test our bounds using the selected feasible datasets. The specific parameters used for each dataset is detailed in Table 1.

Once suitable datasets were selected, the data from each dataset was preprocessed and scaled as discussed in Section 4. The data is then split into training and test datasets using the same split as for the training and validation datasets when selecting feasible datasets for consistency. The SVM model is then trained using this initial  $C_0$ , and the margin is extracted. A similar pipeline as discussed in Section 4 is used.

The training set is passed through a quantum circuit composed of two qubits and  $L$  layers of unitary gates, where each layer corresponds to a layer of IQP encoding gates. The number of unitary layers used in this quantum circuit is dataset-dependent and outlined in Table 1.

All numerical experiments are conducted using *Pennylane* [38]. For this experiment, the quantum circuit, depicted in Figure 7, was again modified to incorporate local depolarising noise channels using Pennylane’s *qml.DepolarizingChannel* function. As discussed in Section 4, noise channels are applied to each qubit after each unitary layer.

A quantum kernel is obtained for increasing levels of noise using this quantum circuit and used to train the classical SVM model from which the noisy margin is extracted. The tunable parameter,  $\beta$  was set to the value of 0 in equation (63) and used to compute the theoretical  $C$  value for the Heart and Gaussian datasets and was set to 1 for the remaining datasets.

Notably, when we discuss the noisy margin, we refer to the margin obtained in the following way. We initially train an SVM model using a kernel matrix obtained from a noisy quantum circuit. This model then solves an optimisation problem and returns a dual solution. We then store this solution, resulting from the noisy kernel matrix and compute the geometric margin with the ideal kernel matrix resulting from the ideal circuit. This is computed using the inverse of the squared norm of the weight vector, as described in Section 3.

This method is used since it adequately describes how noise impacts the geometric margin value, which strongly correlates with generalisation performance as discussed in Section 4. This method tests how well SVM models that are trained in the presence of noise can generalise. It effectively tests how much *useful information* survives in the kernel matrix during training and whether the model is still able to learn patterns from this

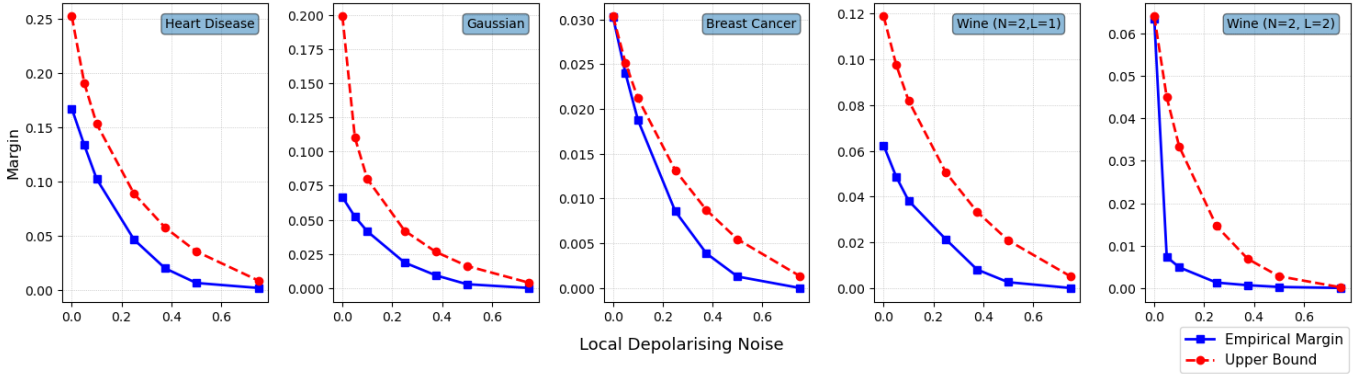


Figure 11: Plots showing the theoretical upper bounds (red) computed for increasing values of local depolarising noise compared to the empirical geometric margin (blue) obtained for various datasets. Each dataset is labelled at the top-right corner of each plot. The values,  $N$  and  $L$ , for the Wine dataset indicate the differing number of qubits and unitary layers used in the quantum circuit, respectively. All unlabelled datasets used two qubits with one unitary layer.

partially noisy matrix. This approach isolates the learning ability and portrays how robust the model is when learning in the presence of noise.

The noisy dual solution is tested in reference to the clean kernel. Interestingly, if we were to obtain the margin with the noisy kernel, we would not see this decay, as the noisy dual solution, while being ineffective with regards to the clean kernel, is optimised for the noisy kernel. As a result, this would not describe the effect of noise on the ideal geometric margin. This would just result in the artificial inflation of the noisy margin value as the solver struggles to find a suitable margin in the face of noisy data.

Using the setup described above, the upper bounds presented by equation (42) were tested using five datasets. A brief description of each dataset is provided in Appendix A.5. Clearly, the theoretical bounds produce an upper bound to the empirical margins computed for these datasets. Figure 11 portrays the results of these tests.

Thereafter, the lower bounds presented by equation (56) were tested in accordance with the above-mentioned constraints. For these specific datasets, this resulted in the datasets being tested with the condition  $\gamma_\alpha^2 C m < \frac{1}{2} \leq (1 - p)^{2N}$ . Figure 12 shows that for the allowed range of local noise values, the bound pro-

duced smaller values than the empirical margin for all five datasets.

In addition to this, a subset of 20 points from the Breast Cancer dataset was selected and used to compare the empirical geometric margin value from the real IBM device with 10000 shots, with our simulated and theoretical values. In particular, the 20 points correspond to the 200th- to 220th-placed samples in the dataset. This subset yielded a feasible  $C'$  range of  $[0, 16.8)$ . This particular slice was selected primarily due to its small size and feasibility with the above-mentioned constraints. The geometric margin was obtained using the software development kit, Qiskit [39] and the ibm\_fez device [40], which is one of the IBM Heron processors. One unitary layer and two qubits were used with identical pre-processing methods as discussed in Section 4. A unitary layer of gates corresponding to IQP encoding was similarly used to maintain consistency. The empirical margin with the theoretical upper and lower bounds was then simulated using the above conditions, for increasing local depolarising noise similar to previous experiments depicted in Figures 11 and 12. The parameters  $C_0 = 1000$ ,  $\beta = 3$  and  $m = 12$  were used in equation (63) to compute the theoretical  $C$  value. The results are presented in Figure 13.

Since the precise level of local depolarising noise is

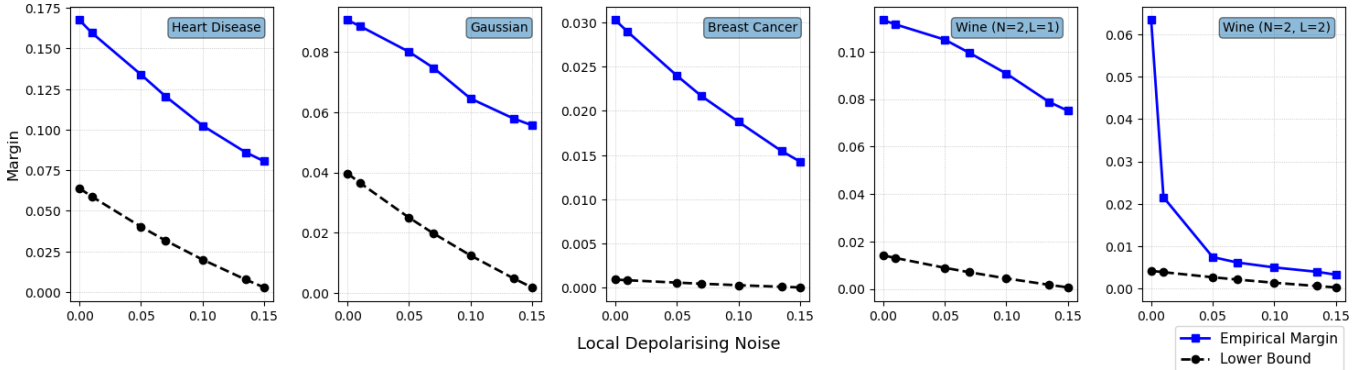


Figure 12: Plots showing the theoretical lower bounds (black) computed for increasing values of local depolarising noise compared to the empirical geometric margin (blue) obtained for various datasets. Each dataset is labelled at the top-right corner of each plot. The values,  $N$  and  $L$ , for the Wine dataset indicate the differing number of qubits and unitary layers used in the quantum circuit, respectively. All unlabelled datasets used two qubits with one unitary layer.

unknown from the real IBM device, we depict the geometric margin as a horizontal green dashed line. The upper and lower bounds are depicted as red and black lines, with the empirical geometric margins simulated for various noise levels depicted by the solid blue line.

Figure 13 suggests that the upper bound is valid for this particular dataset for all values less than the local depolarising noise probability of approximately 0.75. Similarly, the lower bounds appear to be valid for noise values greater than 0.1, since this is where the lower bound crosses the horizontal line representing the margin obtained using real hardware.

Notably, this does not suggest that the upper or lower bounds are invalid. They are simply valid for a particular level of noise. Hence, these results merely suggest that the noise level associated with the quantum device (real device noise) is within the particular noise range for which the bounds are not violated.

## 8 Conclusion

In this work, we presented numerical evidence demonstrating a strong correlation between margin-based metrics and generalisation performance for QSVMs. In particular, we show strong correlations between the median geometric margin value and the test

accuracy obtained for four datasets. A range of datasets with different properties was selected to ensure reliable results. We show evidence that the margin distribution becomes negatively skewed with an increase in training label corruption, as evidenced by the shrinking median margin value. Furthermore, we show a similar decrease in test accuracy with increasingly corrupted labels for all datasets. Following this, we perform linear regression to determine the relationship between test accuracy and the median geometric margin and discover strong linear correlations, coupled with high Pearson correlation coefficients ( $r > 0.9$ ) for all datasets. With these findings, we conclude that the median geometric margin appears to be a reliable indicator of generalisation performance for QSVMs.

Additionally, we motivate the study of local over global depolarising noise despite its analytical intractability for large system sizes. This is supported by empirical results obtained for three datasets, showing that global test accuracy is greater than local test accuracy for intermediate noise levels for the same survival probability. This suggests that global depolarising noise is overly optimistic and does not realistically reflect the generalisation performance degradation and errors due to noise on real device hardware.

Motivated by this, we derive bounds for the effect of

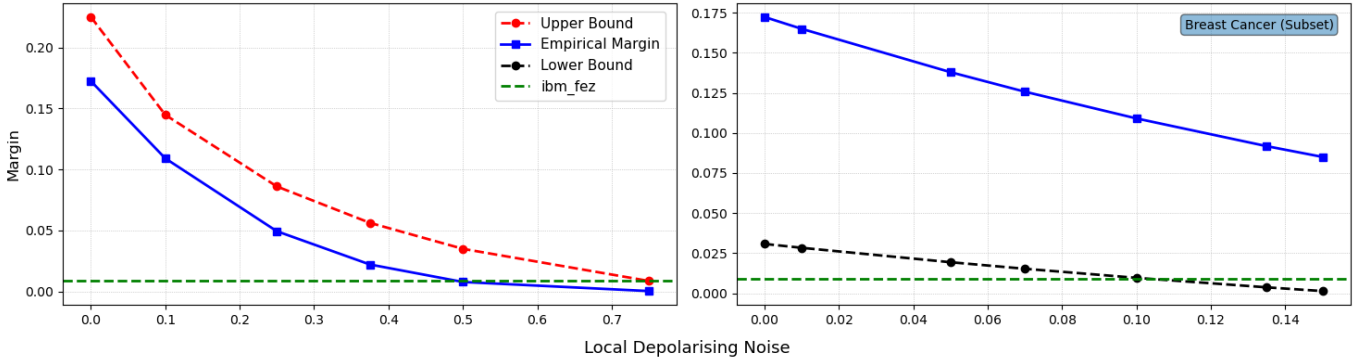


Figure 13: Plots demonstrating comparing the geometric margin obtained using the `ibm_fez` device (depicted by the green dashed line) to the simulated empirical margin (blue) and the theoretical upper and lower bounds (depicted as black and red dashed lines, respectively). These plots were generated using a subset of 20 samples using the Breast Cancer Dataset with 10000 shots.

local depolarising noise on kernel elements. We then use this kernel bound to derive upper and lower bounds on the degradation of the geometric margin due to local depolarising noise. This is obtained by evaluating the dual solution returned by the SVM trained on noisy kernel matrices with respect to the ideal kernel matrix. This method determines the robustness of the QSVM when training in the presence of noise. We conclude by presenting numerical results to validate our margin bounds using five datasets with varying properties. These results include a subset of the Breast Cancer dataset, tested on the `ibm_fez` device, allowing for comparison with our theoretical and simulated margin values.

## Acknowledgements

This research was supported by the National Research Foundation (NRF) of South Africa. The authors would like to acknowledge the National Institute for Theoretical and Computational Sciences (NITheCS). We thank the University of KwaZulu-Natal (UKZN) for the use of the HEP1 machine. We acknowledge the South African Quantum Technology Initiative (SA QuTI) and IBM Quantum services for this work. The views expressed are those of the authors, and do not reflect the official policy or position of IBM or the IBM Quantum team.

## Conflict of Interest

The authors declare no conflict of interest.

## Data Availability Statement

The Gaussian dataset was generated using scikit-learn. All other datasets used in this study were obtained from the UCI Machine Learning Repository [41].

## Code Availability

The code associated with this work is available at [https://github.com/saarishag/generalisation\\_bounds\\_nisq](https://github.com/saarishag/generalisation_bounds_nisq).

## References

- [1] Maria Schuld, Ilya Sinayskiy, and Francesco Petruccione. An introduction to quantum machine learning. *Contemporary Physics*, 56(2):172–185, 2015.
- [2] John Langford and John Shawe-Taylor. Pac-bayes & margins. *Advances in neural information processing systems*, 15, 2002.

[3] Ralf Herbrich and Thore Graepel. A pac-bayesian margin bound for linear classifiers: Why svms work. *Advances in neural information processing systems*, 13, 2000.

[4] David McAllester. Simplified pac-bayesian margin bounds. In *Learning Theory and Kernel Machines: 16th Annual Conference on Learning Theory and 7th Kernel Workshop, COLT/Kernel 2003, Washington, DC, USA, August 24-27, 2003. Proceedings*, pages 203–215. Springer, 2003.

[5] Afshin Rostamizadeh Mehryar Mohri and Ameet Talwalkar. *Foundations of Machine Learning*, 2nd ed. MIT Press, 2018.

[6] Allan Grønlund, Lior Kamma, and Kasper Green Larsen. Near-tight margin-based generalization bounds for support vector machines. In *International Conference on Machine Learning*, pages 3779–3788. PMLR, 2020.

[7] Peter Bartlett and John Shawe-Taylor. Generalization performance of support vector machines and other pattern classifiers. *Advances in Kernel methods—support vector learning*, pages 43–54, 1999.

[8] Vladimir Vapnik. On the uniform convergence of relative frequencies of events to their probabilities. In *Doklady Akademii Nauk USSR*, volume 181, pages 781–787, 1968.

[9] Vladimir Vapnik and Olivier Chapelle. Bounds on error expectation for support vector machines. *Neural computation*, 12(9):2013–2036, 2000.

[10] Vladimir Vapnik. *Estimation of dependences based on empirical data*. Springer Science & Business Media, 2006.

[11] Corinna Cortes and Vladimir Vapnik. Support-vector networks. *Machine learning*, 20(3):273–297, 1995.

[12] John Preskill. Quantum computing in the nisq era and beyond. *Quantum*, 2:79, 2018.

[13] Matthias C Caro, Hsin-Yuan Huang, Marco Cerezo, Kunal Sharma, Andrew Sornborger, Lukasz Cincio, and Patrick J Coles. Generalization in quantum machine learning from few training data. *Nature communications*, 13(1):4919, 2022.

[14] Elies Gil-Fuster, Jens Eisert, and Carlos Bravo-Prieto. Understanding quantum machine learning also requires rethinking generalization. *Nature Communications*, 15(1):2277, 2024.

[15] Tak Hur and Daniel K Park. Understanding generalization in quantum machine learning with margins. In *Forty-second International Conference on Machine Learning*, 2024.

[16] Xinbiao Wang, Yuxuan Du, Yong Luo, and Dacheng Tao. Towards understanding the power of quantum kernels in the nisq era. *Quantum*, 5:531, 2021.

[17] Yabo Wang, Bo Qi, Xin Wang, Tongliang Liu, and Daoyi Dong. Power characterization of noisy quantum kernels. *IEEE Transactions on Neural Networks and Learning Systems*, 2025.

[18] Bikram Khanal, Pablo Rivas, Arun Sanjel, Korn Sooksatra, Ernesto Quevedo, and Alejandro Rodriguez. Generalization error bound for quantum machine learning in nisq era—a survey. *Quantum Machine Intelligence*, 6(2):90, 2024.

[19] Michael A Nielsen and Isaac L Chuang. *Quantum computation and quantum information*. Cambridge university press, 2010.

[20] Peter L Bartlett and Shahar Mendelson. Rademacher and gaussian complexities: Risk bounds and structural results. *Journal of Machine Learning Research*, 3(Nov):463–482, 2002.

[21] Matthias C Caro and Ishaun Datta. Pseudo-dimension of quantum circuits. *Quantum Machine Intelligence*, 2(2):14, 2020.

[22] Leonardo Banchi, Jason Pereira, and Stefano Piandola. Generalization in quantum machine learning: A quantum information standpoint. *PRX Quantum*, 2(4):040321, 2021.

[23] Tobias Haug and M. S. Kim. Generalization of quantum machine learning models using quantum fisher information metric. *Phys. Rev. Lett.*,

133:050603, Jul 2024. doi: 10.1103/PhysRevLett.133.050603. URL <https://link.aps.org/doi/10.1103/PhysRevLett.133.050603>.

[24] Kaifeng Bu, Dax Enshan Koh, Lu Li, Qingxian Luo, and Yaobo Zhang. Statistical complexity of quantum circuits. *Physical Review A*, 105(6):062431, 2022.

[25] Kaifeng Bu, Dax Enshan Koh, Lu Li, Qingxian Luo, and Yaobo Zhang. Effects of quantum resources and noise on the statistical complexity of quantum circuits. *Quantum Science and Technology*, 8(2):025013, 2023.

[26] Kaifeng Bu, Dax Enshan Koh, Lu Li, Qingxian Luo, and Yaobo Zhang. Rademacher complexity of noisy quantum circuits. *arXiv preprint arXiv:2103.03139*, 2021.

[27] Chiyuan Zhang, Samy Bengio, Moritz Hardt, Benjamin Recht, and Oriol Vinyals. Understanding deep learning (still) requires rethinking generalization. *Communications of the ACM*, 64(3):107–115, 2021.

[28] Peter L Bartlett, Dylan J Foster, and Matus J Telgarsky. Spectrally-normalized margin bounds for neural networks. *Advances in neural information processing systems*, 30, 2017.

[29] Supanut Thanasilp, Samson Wang, Marco Cerezo, and Zoë Holmes. Exponential concentration in quantum kernel methods. *Nature communications*, 15(1):5200, 2024.

[30] Bernhard E Boser, Isabelle M Guyon, and Vladimir N Vapnik. A training algorithm for optimal margin classifiers. In *Proceedings of the fifth annual workshop on Computational learning theory*, pages 144–152, 1992.

[31] Maria Schuld and Nathan Killoran. Quantum machine learning in feature hilbert spaces. *Physical review letters*, 122(4):040504, 2019.

[32] Robert J Lyon, BW Stappers, Sally Cooper, John Martin Brooke, and Joshua D Knowles. Fifty years of pulsar candidate selection: from simple filters to a new principled real-time classification approach. *Monthly Notices of the Royal Astronomical Society*, 459(1):1104–1123, 2016.

[33] Vojtěch Havlíček, Antonio D Córcoles, Kristan Temme, Aram W Harrow, Abhinav Kandala, Jerry M Chow, and Jay M Gambetta. Supervised learning with quantum-enhanced feature spaces. *Nature*, 567(7747):209–212, 2019.

[34] Daniel Berrar et al. Cross-validation., 2019.

[35] Svante Wold, Kim Esbensen, and Paul Geladi. Principal component analysis. *Chemometrics and intelligent laboratory systems*, 2(1-3):37–52, 1987.

[36] Yuxuan Du, Min-Hsiu Hsieh, Tongliang Liu, Shan You, and Dacheng Tao. Learnability of quantum neural networks. *PRX quantum*, 2(4):040337, 2021.

[37] Davide Anguita, Alessandro Ghio, Sandro Ridella, and Dario Sterpi. K-fold cross validation for error rate estimate in support vector machines. In *DMIN*, pages 291–297, 2009.

[38] Ville Bergholm, Josh Izaac, Maria Schuld, Christian Gogolin, Shahnawaz Ahmed, Vishnu Ajith, M Sohaib Alam, Guillermo Alonso-Linaje, B Akash-Narayanan, Ali Asadi, et al. PennyLane: Automatic differentiation of hybrid quantum-classical computations. *arXiv preprint arXiv:1811.04968*, 2018.

[39] Ali Javadi-Abhari, Matthew Treinish, Kevin Krsulich, Christopher J. Wood, Jake Lishman, Julien Gacon, Simon Martiel, Paul D. Nation, Lev S. Bishop, Andrew W. Cross, Blake R. Johnson, and Jay M. Gambetta. Quantum computing with Qiskit, 2024.

[40] IBM Quantum. <https://quantum.cloud.ibm.com/>, 2025.

[41] Kolby Nottingham Markelle Kelly, Rachel Longjohn. The uci machine learning repository. <https://archive.ics.uci.edu/>, 1987.

# A Appendix

## A.1 Kernel Bound ( $L$ Layers)

In this section, we present bounds for the case of kernel elements affected by  $L$  applications of a local depolarising noise channel for an  $N$ -qubit system.

Before we rework our bound to include  $L$  layers, it would be beneficial to recall that quantum circuit is modelled using the sequential composition of quantum channels as  $\mathcal{E}^{(L)} = \mathcal{E}^{(L)} \circ \dots \circ \mathcal{E}^{(1)}$ . In the Kraus representation, this translates to the product of Kraus operators over  $L$  layers.

For a single-qubit, the state after applying  $L$  local depolarising channels can be written as:

$$\mathcal{E}(\rho) = \sum_{m \in \{0,1,2,3\}} \left( \prod_{l=1}^L K_m^{(l)} \right) \rho \left( \prod_{l=1}^L K_m^{(l)} \right)^\dagger \quad (64)$$

where  $K_m^{(l)}$  represents the single-qubit Kraus operators defined by the expressions in 15 acting at layer  $l$ .

This naturally extends to an  $N$ -qubit system by taking the tensor product of the single-qubit Kraus operators across the  $N$  qubits at each layer.

We can now begin our derivation of the kernel bounds for  $N$  qubits and  $L$  layers. Analogous to the single-layer bound, we first take ratio of the  $ij$ 'th noisy kernel element with its corresponding noiseless element.

$$\frac{\tilde{K}_{ij}}{K_{ij}} = \frac{\text{Tr}(\tilde{\rho}_i \tilde{\rho}_j)}{\text{Tr}(\rho_i \rho_j)} \quad (65)$$

where  $\tilde{\rho}_i$  represents the noisy density matrix representing the state after the application of the noisy depolarising channels.

Now, we substitute the expression for the noisy density matrix and using the linearity property of the trace operator. Additionally, we use the cyclic properties of the trace operator and note that the Kraus operators defined in 15 are Hermitian ( $K = K^\dagger$ ), due to the Pauli matrices also being Hermitian to obtain:

$$\begin{aligned} \frac{\tilde{K}_{ij}}{K_{ij}} &= (1-p)^{2LN} + \frac{1}{\text{Tr}(\rho_i \rho_j)} \sum_{\substack{\mathbf{m}, \mathbf{n} \in \{0,1,2,3\}^N \\ (\mathbf{m}, \mathbf{n} \neq 0)}} \text{Tr} \\ &\left( \rho_i \left( \prod_{l=1}^L \left( \bigotimes_{k=1}^N K_{m_k}^{(l)} K_{n_k}^{(l)} \right) \right) \rho_j \left( \prod_{l=1}^L \left( \bigotimes_{k=1}^N K_{n_k}^{(l)} K_{m_k}^{(l)} \right) \right) \right) \end{aligned} \quad (66)$$

The first term is as a result of separating the  $\mathbf{m} = \mathbf{n} = 0$  term from the rest of the sum and substituting the definition of the Kraus operator,  $K_0$ .

From this equation, we note that the first term is the probability of the kernel element remaining unchanged after the application of the noise channel, while the second term is the contribution due to noise.

Now, we bound the noisy contribution, defined by  $\tilde{N}$ , and write it in the form

$$\tilde{N} = \frac{1}{\text{Tr}(\rho_i \rho_j)} \sum_{\substack{\mathbf{m}, \mathbf{n} \in \{0,1,2,3\}^N \\ (\mathbf{m}, \mathbf{n} \neq 0)}} \text{Tr}(\rho_i Q_{mn} \rho_j Q_{nm}) \quad (67)$$

where, we define

$$Q_{mn} = \bigotimes_{k=1}^N \left( \prod_{l=1}^L K_{m_k}^{(l)} K_{n_k}^{(l)} \right)$$

Now, we note that for some  $\alpha, \beta \in \{0, 1, 2, 3\}$ ,

$$K_\alpha^{(l)} K_\beta^{(l)} = c_{\alpha\beta}^{(l)} \sigma_\alpha^{(l)} \sigma_\beta^{(l)}$$

The piecewise function for the constants  $c_{\alpha\beta}^{(l)}$  are defined similarly as in the  $L = 1$  case.

From this, it is clear that we find that:

$$Q_{mn} = \prod_{k=1}^N \prod_{l=1}^L c_{m_k n_k}^{(l)} \bigotimes_{k=1}^N (\sigma_{m_k}^{(l)} \sigma_{n_k}^{(l)}) = Q_{nm}^\dagger$$

Hence, the noisy term can be rewritten as:

$$\tilde{N} = \sum_{\substack{\mathbf{m}, \mathbf{n} \in \{0,1,2,3\}^N \\ (\mathbf{m}, \mathbf{n} \neq 0)}} \prod_{l=1}^L \left( \prod_{k=1}^N (c_{m_k n_k}^{(l)})^2 \right) \frac{1}{\text{Tr}(\rho_i \rho_j)} \text{Tr} \left( \rho_i \left( \bigotimes_{k=1}^N \sigma_{m_k}^{(l)} \sigma_{n_k}^{(l)} \right) \rho_j \left( \bigotimes_{k=1}^N \sigma_{n_k}^{(l)} \sigma_{m_k}^{(l)} \right) \right) \quad (68)$$

The next steps follow similarly as in the  $L = 1$  case.

Hence, the noisy contribution becomes

$$\tilde{N} \leq \sum_{\substack{\mathbf{m}, \mathbf{n} \in \{0,1,2,3\}^N \\ (\mathbf{m}, \mathbf{n} \neq 0)}} \left( \prod_{l=1}^L \prod_{k=1}^N (c_{m_k n_k}^{(l)})^2 \right) \frac{1}{K_{ij}} \quad (69)$$

Thus, the value of the  $ij$ -th kernel element in the kernel matrix is bounded by

$$\tilde{K}_{ij} \leq (1-p)^{2LN} K_{ij} + \sum_{\substack{\mathbf{m}, \mathbf{n} \in \{0,1,2,3\}^N \\ (\mathbf{m}, \mathbf{n} \neq 0)}} \left( \prod_{k=1}^N (c_{m_k n_k}^{(l)})^2 \right)$$

Similarly, by the normalisation condition, we get:

$$\tilde{K}_{ij} \leq (1-p)^{2LN} K_{ij} + (1 - (1-p)^{2LN}) \quad (70)$$

This upper-bounds the resulting kernel element after the local application of  $L$  depolarising noise channels.

## A.2 Local Depolarising Noise on Kernel - Exact Expression

In this section, we derive an exact expression for the noisy kernel affected by 1 layer of local depolarising noise channels for  $N$  qubits.

Recall that we express the state after applying a single local depolarising channel on each qubit in an  $N$ -qubit system using the tensor product of the single-qubit Kraus operators in the following form:

$$\tilde{\rho} = \sum_{\mathbf{m} \in \{0,1,2,3\}^N} \left( \bigotimes_{k=1}^N K_{m_k} \right) \rho \left( \bigotimes_{k=1}^N K_{m_k}^\dagger \right) \quad (71)$$

We now use the density matrix to compute the  $ij$ -th kernel element.

Following a similar procedure as the bound derivation, the resulting expression can be written as

$$\tilde{K}_{ij} = \sum_{\substack{\mathbf{m}, \mathbf{n} \in \\ \{0,1,2,3\}^N}} \text{Tr} \left( \rho_i \left( \bigotimes_{k=1}^N K_{m_k} K_{n_k} \right) \rho_j \left( \bigotimes_{k=1}^N K_{n_k} K_{m_k} \right) \right) \quad (72)$$

We now use density matrix properties to rewrite it in terms of the Pauli matrices. For some density matrix,  $\rho$ :

$$\rho = \frac{1}{2} (\mathbf{r} \cdot \boldsymbol{\sigma}) \quad (73)$$

Here,  $\boldsymbol{\sigma} = (\sigma_0, \sigma_1, \sigma_2, \sigma_3)$  and  $\mathbf{r} = (r_0, r_x, r_y, r_z)$ , where  $r_i = \text{Tr}(\rho \sigma_i)$  for  $i \in \{1, 2, 3\}$ . As usual,  $\sigma_0 = I$ ,  $\sigma_1 = \sigma_x$ ,  $\sigma_2 = \sigma_y$  and  $\sigma_3 = \sigma_z$ .

For  $N$ -qubits, this extends to

$$\rho = \frac{1}{2^N} \sum_{\boldsymbol{\mu} \in \{0,1,2,3\}^N} \mathbf{r}_{\boldsymbol{\mu}} \cdot (\sigma_{\mu_1} \otimes \cdots \otimes \sigma_{\mu_N}) \quad (74)$$

where  $\boldsymbol{\mu} = \{\mu_1, \dots, \mu_N\}$  and  $\mathbf{r}_{\boldsymbol{\mu}} = \text{Tr}(\rho (\sigma_{\mu_1} \otimes \cdots \otimes \sigma_{\mu_N}))$ , where  $\mu_i \in \{0, 1, 2, 3\}$ .

Using this definition, we rewrite the density matrices ( $\rho_i$  and  $\rho_j$ ) in terms of the Pauli matrices.

We then simplify the resulting expression using properties of the tensor product.

$$\begin{aligned} \tilde{K}_{ij} &= \frac{1}{2^{2N}} \sum_{\mathbf{m}, \mathbf{n}, \boldsymbol{\mu}, \boldsymbol{\nu} \in \{0,1,2,3\}^N} r_{\boldsymbol{\mu}}^{(i)} r_{\boldsymbol{\nu}}^{(j)} \\ &\quad \text{Tr} \left( \bigotimes_{k=1}^N (K_{n_k} \sigma_{\nu_k} K_{n_k} K_{m_k} \sigma_{\mu_k} K_{m_k}) \right) \end{aligned} \quad (75)$$

$r_{\boldsymbol{\mu}}^{(i)} r_{\boldsymbol{\nu}}^{(j)}$  are scalars, hence they are taken out of the trace expression.

In order to further simplify this expression, we recall the definition of the Kraus operators for single-qubit local depolarising noise channels.

We consider the  $n_k$  and  $\nu_k$  terms inside the trace expression, for  $k = 1$ .

$$K_{n_1} \sigma_{\nu_1} K_{n_1}$$

Since  $n_1, \nu_1 \in [0, 1, 2, 3]$ , we have the following scenarios.

If  $n_1 = 0$ , then  $K_{n_1} = K_0 = \sqrt{1-p} I$ . Thus here,

$$K_0 \sigma_{\nu_1} K_0 = (1-p) \sigma_{\nu_1}$$

However, if  $n_1 \neq 0$ , then  $K_{n_1} = K_i = \sqrt{p/3} \sigma_i$  for  $i \in [1, 2, 3]$ . In this case:

$$K_i \sigma_{\nu_1} K_i = \frac{p}{3} \sigma_{\nu_1}$$

In light of these cases, we can introduce the following constant:

$$c_{n_1} = \begin{cases} (1-p) & \text{if } n_1 = 0 \\ \frac{p}{3} & \text{if } n_1 \in [1, 2, 3] \end{cases}$$

Now, we similarly attempt to describe the  $\sigma_{\nu_1}$  factor.

$$K_{n_1} \sigma_{\nu_1} K_{n_1} = c_{n_1} \sigma_{n_1} \sigma_{\nu_1} \sigma_{n_1}$$

We first analyse the product of three general Pauli matrices of the form  $\sigma_i \sigma_j \sigma_i$

We use the following result for the product of two Pauli matrices:

$$\sigma_i \sigma_j = \delta_{ij} I + i \epsilon_{ijk} \sigma_k \quad (76)$$

where  $\delta_{ij}$  is the Kronecker delta, which has the definition:

$$\delta_{ij} = \begin{cases} 1, \text{if } i = j \\ 0, \text{else} \end{cases}$$

and  $\epsilon_{ijk}$  is the Levi-Civita symbol, which is defined as:

$$\epsilon_{ijk} = \begin{cases} +1, \text{ for even permutations of } (i, j, k) \\ -1, \text{ for odd permutations of } (i, j, k) \\ 0, \text{ for repeated indices} \end{cases}$$

Using this result to determine the product of three Pauli matrices (where  $\sigma_i \neq \sigma_j$ ), we get:

$$\sigma_i \sigma_j \sigma_i = \sigma_i (\delta_{ji} I + i \epsilon_{jik} \sigma_k)$$

This becomes

$$\sigma_i \sigma_j \sigma_i = -i (\sigma_i \sigma_k)$$

Now applying the result for the product of two Pauli matrices for  $\sigma_i \sigma_k$  gives us:

$$-i (\sigma_i \sigma_k) = -i (\delta_{ik} I + i \epsilon_{ikj} \sigma_j)$$

Simplifying this gives us the following result for the case of  $(i \neq j)$ :

$$\sigma_i \sigma_j \sigma_i = -\sigma_j$$

However, when  $\sigma_i = \sigma_j$ , this easily simplifies to

$$\sigma_i \sigma_j \sigma_i = \sigma_i (\sigma_i)^2 = \sigma_i (I) = \sigma_i \quad (77)$$

Using the above results, we can now introduce a generalised result for the product of three Pauli matrices.

$$\sigma_i \sigma_j \sigma_i = \eta_{ij} \sigma_j \quad (78)$$

where  $\eta_{ij}$  is defined as:

$$\eta_{ij} = \begin{cases} +1, \text{if } j \in \{0, i\} \\ -1, \text{else} \end{cases}$$

We can now rewrite  $K_{n_1} \sigma_{\nu_1} K_{n_1}$  using this relationship as:

$$K_{n_1} \sigma_{\nu_1} K_{n_1} = c_{n_1} \eta_{n_1, \nu_1} \sigma_{\nu_1} \quad (79)$$

Similarly, we can define the expression:  $K_{m_1} \sigma_{\mu_1} K_{m_1} = c_{m_1} \eta_{m_1, \mu_1} \sigma_{\mu_1}$ . Substituting these expressions into 75 results in:

$$\tilde{K}_{ij} = \frac{1}{2^{2N}} \sum_{\mathbf{m}, \mathbf{n}, \mathbf{\mu}, \mathbf{\nu} \in \{0, 1, 2, 3\}^N} r_{\mu}^{(i)} r_{\nu}^{(j)} \left( \bigotimes_{k=1}^N c_{n_k} c_{m_k} \eta_{n_k, \nu_k} \eta_{m_k, \mu_k} \text{Tr} (\sigma_{\nu_k} \sigma_{\mu_k}) \right) \quad (80)$$

To simplify further, we analyse the tensor product of the trace term. Expanding this gives

$$\bigotimes_{k=1}^N \text{Tr} (\sigma_{\nu_k} \sigma_{\mu_k}) = \text{Tr} (\sigma_{\nu_1} \sigma_{\mu_1} \otimes \cdots \otimes \sigma_{\nu_N} \sigma_{\mu_N}) \quad (81)$$

Simplifying using trace properties,  $\text{Tr}(A \otimes B) = \text{Tr}(A) \cdot \text{Tr}(B)$  and  $\text{Tr}(\sigma_i \sigma_j) = 2\delta_{ij}$ .

$$\text{Tr}(\sigma_{\nu_1} \sigma_{\mu_1}) \dots \text{Tr}(\sigma_{\nu_N} \sigma_{\mu_N}) = 2^N \delta_{\nu\mu} \quad (82)$$

We now substitute this into our expression and set  $\nu = \mu$ .

$$\tilde{K}_{ij} = \frac{1}{2^N} \sum_{\substack{\mathbf{m}, \mathbf{n}, \mu, \\ \in \{0, 1, 2, 3\}^N}} r_{\mu}^{(i)} r_{\mu}^{(j)} \left( \prod_{k=1}^N c_{n_k} c_{m_k} \eta_{n_k, \mu_k} \eta_{m_k, \mu_k} \right) \quad (83)$$

where we changed the tensor product to a product over the scalars.

Separating the  $\mathbf{m} = \mathbf{n} = 0$  term from the rest of the sum leaves:

$$\begin{aligned} \tilde{K}_{ij} &= \frac{1}{2^N} (1-p)^{2N} \sum_{\mu \in \{0, 1, 2, 3\}^N} r_{\mu}^{(i)} r_{\mu}^{(j)} + \frac{1}{2^N} \\ &\quad \sum_{\substack{\mathbf{m}, \mathbf{n}, \mu, \in \{0, 1, 2, 3\}^N \\ (\mathbf{m} = \mathbf{n} \neq 0)}} r_{\mu}^{(i)} r_{\mu}^{(j)} \left( \prod_{k=1}^N c_{n_k} c_{m_k} \eta_{n_k, \mu_k} \eta_{m_k, \mu_k} \right) \end{aligned} \quad (84)$$

where

$$\frac{1}{2^N} \sum_{\mu \in \{0, 1, 2, 3\}^N} r_{\mu}^{(i)} r_{\mu}^{(j)}$$

can easily be shown to be the expression for the  $ij$ -th noiseless kernel element,  $K_{ij}$

Thus, the final exact expression for the noisy kernel affected by local depolarising noise is:

$$\begin{aligned} \tilde{K}_{ij} &= (1-p)^{2N} K_{ij} + \frac{1}{2^N} \sum_{\substack{\mathbf{m}, \mathbf{n}, \mu, \in \{0, 1, 2, 3\}^N \\ (\mathbf{m} = \mathbf{n} \neq 0)}} \\ &\quad r_{\mu}^{(i)} r_{\mu}^{(j)} \left( \prod_{k=1}^N c_{n_k} c_{m_k} \eta_{n_k, \mu_k} \eta_{m_k, \mu_k} \right) \end{aligned} \quad (85)$$

Similarly, this can be modified to include the application of  $L$  layers of local depolarising noise channels to  $N$  qubits as detailed in Appendix A.1.

While it is possible to obtain an exact form for the  $ij$ -th noisy kernel element, the above expression lacks a closed-form simplification and the second term becomes analytically-intractable for large  $N$ .

For these reasons, we derive and present bounds for the noisy kernel elements in the main text.

### A.3 Auxiliary Results for Upper Margin Bounds

#### A.3.1 Result 1A

Here we consider the effect of the noisy kernel bounds on the noisy squared weighted norm. The noisy squared weighted norm is defined as:

$$\|\tilde{\mathbf{w}}\|_{\tilde{\alpha}}^2 = \sum_{i,j} \tilde{\alpha}_i \tilde{\alpha}_j y_i y_j \tilde{K}_{ij} \quad (86)$$

Substituting the noisy kernel bounds gives us:

$$\|\tilde{\mathbf{w}}\|_{\tilde{\alpha}}^2 \leq (1-p)^{2N} \sum_{i,j} \tilde{\alpha}_i \tilde{\alpha}_j y_i y_j K_{ij} + (1 - (1-p)^{2N}) \sum_{i,j} \tilde{\alpha}_i \tilde{\alpha}_j y_i y_j$$

The second KKT condition reduces this inequality to the form:

$$\|\tilde{\mathbf{w}}\|_{\tilde{\alpha}}^2 \leq (1-p)^{2N} \sum_{i,j} \tilde{\alpha}_i \tilde{\alpha}_j y_i y_j K_{ij} \quad (87)$$

Comparing this form with its noiseless counterpart, we see that it can be rewritten as

$$\|\tilde{\mathbf{w}}\|_{\tilde{\alpha}}^2 \leq (1-p)^{2N} \|\mathbf{w}\|_{\tilde{\alpha}}^2 \quad (88)$$

where we define

$$\|\mathbf{w}\|_{\tilde{\alpha}}^2 = \sum_{i,j} \tilde{\alpha}_i \tilde{\alpha}_j y_i y_j K_{ij}$$

This is just the definition of the squared norm of the weight with the noiseless kernel values and noisy Lagrangian variables ( $\tilde{\alpha}$ ) used instead of the noiseless alternative.

#### A.3.2 Result 1B

Similarly, we can construct a bound for the squared weighted norm that uses noisy kernel values with clean Lagrangian variables. This quantity has the form:

$$\|\tilde{\mathbf{w}}\|_{\alpha}^2 = \sum_{i,j} \alpha_i \alpha_j y_i y_j \tilde{K}_{ij} \quad (89)$$

$$\|\tilde{\mathbf{w}}\|_{\alpha}^2 \leq \sum_{i,j} \alpha_i \alpha_j y_i y_j [(1-p)^{2N} K_{ij} + (1 - (1-p)^{2N})] \quad (90)$$

As with Result 1A, this can be simplified using the KKT conditions and rewritten using the noiseless definition of the squared weighted norm as:

$$\|\tilde{\mathbf{w}}\|_{\alpha}^2 \leq (1-p)^{2N} \|\mathbf{w}\|_{\alpha}^2 \quad (91)$$

### A.3.3 Result 2

Starting with the complementarity condition (expressed by the fourth KKT condition), we have:

$$y_i(\mathbf{w} \cdot \phi(\mathbf{x}_i) + b) = 1 - \xi_i \quad (92)$$

By multiplying both sides by  $\alpha_i$  and taking the sum, we get:

$$\sum_{i=1}^m \alpha_i y_i (\mathbf{w} \cdot \phi(\mathbf{x}_i) + b) = \sum_{i=1}^m \alpha_i (1 - \xi_i) \quad (93)$$

Simplifying and applying the KKT conditions results in:

$$\sum_{i=1}^m \alpha_i y_i \mathbf{w} \cdot \phi(\mathbf{x}_i) = \sum_{i=1}^m \alpha_i - \sum_{i=1}^m \alpha_i \xi_i \quad (94)$$

The term on the LHS is exactly the squared weighted norm. We show this by using its definition to get:

$$\|\mathbf{w}\|^2 = \mathbf{w} \cdot \mathbf{w} \quad (95)$$

$$\|\mathbf{w}\|^2 = \mathbf{w} \cdot \sum_{i=1}^m \alpha_i y_i \phi(\mathbf{x}_i) \quad (96)$$

which can be rewritten as:

$$\|\mathbf{w}\|^2 = \sum_{i=1}^m \alpha_i y_i \mathbf{w} \cdot \phi(\mathbf{x}_i) \quad (97)$$

Substituting this definition into the above equation and rewriting the squared weight norm for notation consistency gives:

$$\|\alpha\|_1 = \|\mathbf{w}\|_{\alpha}^2 + \sum_{i=1}^m \alpha_i \xi_i \quad (98)$$

We now apply the KKT condition for the non-separable data case for which  $\alpha_i = C$  when  $\xi_i \neq 0$ , to get:

$$\|\alpha\|_1 = \|\mathbf{w}\|_{\alpha}^2 + C \sum_{i=1}^m \xi_i \quad (99)$$

Consequently, this results in the relation:

$$\|\mathbf{w}\|_{\alpha}^2 \leq \|\alpha\|_1 \quad (100)$$

### A.3.4 Result 3

We now construct a bound for the sum of the slack variables  $\sum_{i=1}^m \xi_i$ .

First, we recap the primal optimisation problem (with  $p = 1$ ):

$$P = \min_{\mathbf{w}, b, \xi} \frac{1}{2} \|\mathbf{w}\|^2 + C \sum_{i=1}^m \xi_i \quad (101)$$

which is subject to the following constraints:

$$y_i(\mathbf{w} \cdot \phi(\mathbf{x}_i) + b) \geq 1 - \xi_i \text{ and } \xi_i \geq 0 \text{ for } i \in [1, m]$$

We can now construct a trivial solution for the optimisation problem. To do this, we choose the solution  $(\mathbf{w}^* = \mathbf{0}, b^* = 0, \xi^* = 1)$ .

Clearly, the trivial solution always satisfies the above constraints and is hence a feasible solution for this optimisation problem.

Evaluating the primal objective function using this trivial solution results in

$$P(\mathbf{w}^*, b^*, \xi^*) = \frac{1}{2} \|\mathbf{0}\|^2 + C \sum_{i=1}^m 1 = mC$$

Let  $(\mathbf{w}, b, \xi)$  denote the optimal solution to the above primal optimisation problem, which takes the form

$$P(\mathbf{w}, b, \xi) = \frac{1}{2} \|\mathbf{w}\|^2 + C \sum_{i=1}^m \xi_i \quad (102)$$

Due to optimality, the primal objective function evaluated at the optimal solution must be at most the value of the function evaluated at any other feasible solution (such as our trivial solution). Hence, we have the relation:

$$P(\mathbf{w}, b, \xi) \leq P(\mathbf{w}^* = \mathbf{0}, b^* = 0, \xi^* = \mathbf{1}) \quad (102)$$

This reveals the following relation:

$$\frac{1}{2} \|\mathbf{w}\|^2 + C \sum_{i=1}^m \xi_i \leq mC \quad (103)$$

Since  $\frac{1}{2} \|\mathbf{w}\|^2 \geq 0$ , we get:

$$C \sum_{i=1}^m \xi_i^* \leq mC \quad (104)$$

## A.4 Auxiliary Results for Lower Margin Bounds

### A.4.1 Result 1

Here, we prove the analogous relation to that found in Section A.3.3 using the noisy dual solution with the noiseless kernel.

Similar to the noiseless analogue, we start with the complementarity condition:

$$y_i(\mathbf{w}_{\tilde{\alpha}} \cdot \phi(\mathbf{x}_i) + \tilde{b}) = 1 - \zeta_i$$

We then multiply both sides by  $\tilde{\alpha}_i$  and take the sum. After applying KKT conditions, we get:

$$\sum_{i=1}^m \tilde{\alpha}_i y_i (\mathbf{w}_{\tilde{\alpha}} \cdot \phi(\mathbf{x}_i)) = \sum_{i=1}^m \tilde{\alpha}_i - \sum_{i=1}^m \tilde{\alpha}_i \zeta_i$$

Similarly, the LHS is exactly the squared norm of the weight vector. After applying the KKT condition stating that if  $\zeta_i \neq 0$ ,  $\tilde{\alpha}_i = C$ , else  $\zeta_i = 0$ , we get:

$$\|\mathbf{w}\|_{\tilde{\alpha}}^2 = \|\tilde{\alpha}\|_1 - C \sum_{i=1}^m \zeta_i$$

Finally, we get the following relationship:

$$\|\tilde{\alpha}\|_1 = \|\mathbf{w}\|_{\tilde{\alpha}}^2 + C \sum_{i=1}^m \zeta_i \quad (105)$$

### A.4.2 Result 2

An analogous relation to that found in Section A.4.1 can be constructed for the noisy kernel and noisy dual solution as:

$$\|\tilde{\alpha}\|_1 = \|\tilde{\mathbf{w}}\|_{\tilde{\alpha}}^2 + C \sum_{i=1}^m \tilde{\xi}_i \quad (106)$$

Clearly, we can equate both results to obtain the relation

$$\|\tilde{\mathbf{w}}\|_{\tilde{\alpha}}^2 + C \sum_{i=1}^m \tilde{\xi}_i = \|\mathbf{w}\|_{\tilde{\alpha}}^2 + C \sum_{i=1}^m \zeta_i$$

Finally, rearranging this gives:

$$C \sum_{i=1}^m \zeta_i = \|\tilde{\mathbf{w}}\|_{\tilde{\alpha}}^2 - \|\mathbf{w}\|_{\tilde{\alpha}}^2 + C \sum_{i=1}^m \tilde{\xi}_i \quad (107)$$

## A.5 About the Datasets

In this section, we provide more details relating to the initial preparation of the datasets to be used for the numerical simulations.

As mentioned in the main text, the Heart Disease, (White) Wine, HTRU2, and Breast Cancer datasets were obtained using the UCI Machine Learning Repository [41].

**(White) Wine Dataset** This dataset includes white vinho verde wine samples, with the target variable containing values quantifying wine quality. Wine quality contained multiple classes, with values ranging from 3 to 9.

We categorise all samples with wine quality scores of above 5 as premium quality wine, and the remaining samples as standard quality wine. We then defined all premium quality wine to form the binary class 1, with standard quality wine forming class 0, thereby transforming this dataset for a binary classification task.

**Heart Disease Dataset** The heart disease dataset consists of 13 features and 1 target variable. Similar to the Wine Quality dataset, this target variable contained multiple values, ranging from 0 to 4, where the values  $\in [1, 4]$ , indicated the presence of heart disease in the particular patient, with 0 indicating the absence of heart disease. The target variable has similarly been

transformed for binary classification by defining all samples with heart diseases scores above 0 as class 1, with samples with scores of 0 used to form class 0. This allows the dataset to be separated into samples of patients who have heart disease, and those who do not. Additionally, this dataset initially had 6 missing values; 2 and 4 values two features, respectively. These missing values were imputed with the median value from each feature vector using *sklearn's SimpleImputer*.

**Breast Cancer Dataset** This dataset contains a 9 features and 1 binary target variable with values "M" or "B" labelling if a tumour is malignant or benign. This column was also transformed for binary classification by mapping malignant and benign tumours to the values 1 and 0, respectively.

**HTRU2 Dataset** The HTRU2 dataset contains pulsar candidates from the HTRU2 (South) survey. This dataset consists of 7 feature vectors and 1 binary target variable. This target variable takes the value of 1 for pulsars and 0 if not.

**Gaussian Dataset** The Gaussian dataset was curated using scikit-learn's *make\_blobs* function. This function is used to generate isotropic Gaussian blobs representing the two classes for binary classification. This distribution was generated with a cluster standard deviation of 3. Larger values for the cluster standard deviation result in a higher degree of overlap between the two classes resulting in non-linearly separable data.